

# On the estimation of boundary layer heights: A machine learning approach

Raghavendra Krishnamurthy<sup>1</sup>, Rob K. Newsom<sup>1</sup>, Larry K. Berg<sup>1</sup>, Heng Xiao<sup>1</sup>, Po-Lun Ma<sup>1</sup>, David D. Turner<sup>2</sup>

5 <sup>1</sup>Pacific Northwest National Laboratory, ASGC Division, Richland, 99354, USA

<sup>2</sup>National Oceanic and Atmospheric Administration / Global Systems Laboratory, Boulder, 80305, USA

*Correspondence to:* Raghavendra Krishnamurthy (raghu@pnnl.gov)

**Abstract.** The planetary boundary-layer height ( $z_i$ ) is a key parameter used in atmospheric models for estimating the exchange of heat, momentum and moisture between the surface and the free troposphere. Near-surface atmospheric and subsurface properties (such as soil temperature, relative humidity etc.) are known to have an impact on  $z_i$ . Nevertheless, precise relationships between these surface properties and  $z_i$  are less well known and not easily discernible from the **multi-year dataset**. Machine learning approaches, such as Random Forest (RF), which use a multi-regression framework, help to decipher some of the physical processes linking surface-based characteristics to  $z_i$ . In this study, a **four-year** dataset from 2016 to 2019 at the Southern Great Plains site is used to develop and test a machine learning framework for estimating  $z_i$ . Parameters derived from Doppler lidars are used in combination with over 20 different surface meteorological measurements as inputs to a RF model. The model is trained using radiosonde-derived  $z_i$  values spanning the period from 2016 through 2018, and then evaluated using data from 2019. Results from 2019 showed significantly better agreement with the radiosonde compared to estimates derived from a thresholding technique using Doppler lidars **only**. **Noteworthy improvements in daytime  $z_i$  estimates were observed using the RF model, with a 50% improvement in mean absolute error and an  $R^2$  of greater than 85% compared to the Tucker method  $z_i$ .** We also explore the effect of  $z_i$  uncertainty on convective velocity scaling and present preliminary comparisons between the RF model and  $z_i$  estimates derived from atmospheric models.

## 1 Introduction

25 Measuring the growth of the Planetary Boundary Layer (PBL) height is crucial for understanding the turbulent transfer of air mass, which in turn strongly influences the winds, temperature, and moisture within the atmospheric boundary layer. During daytime, the air within the PBL is well mixed due to convection and results in weakening of turbulence at the top of the PBL (entrainment zone). **One of the characteristics of the top of the PBL during clear sky conditions is that the turbulence is near zero, while in cases with boundary-layer clouds, significant up and downdrafts can be observed at the top of the**

30 **boundary layer (typically the cloud base height)**. Routine, continuous, long-term monitoring of the PBL height,  $z_i$ , is crucial for evaluating climate, weather, and air quality models skill in representing near-surface turbulent mixing, entrainment across the PBL top, the development of shallow cumulus, **understanding** effects of morning or evening transitions (Grant 1997), and nocturnal convection initiation (Reif et al., 2017). Profiles of potential temperature, water vapor mixing ratio, and particulate concentration often exhibit strong gradients at or near the top of the PBL. Typically, estimates of  $z_i$  are obtained from an analysis of temperature and humidity profiles obtained from radiosondes. Indeed, radiosondes continue to be the **de facto** standard due to their long operational history, **fine vertical resolution**, accuracy, and reliability. However, major limitations are the poor temporal resolution and large sampling error **because** radiosondes are typically only launched twice daily at operational centers around the world. The launch time periods are generally not optimal for looking at various boundary layer properties. As a result, the diurnal variation in  $z_i$  is usually poorly represented in radiosonde data.

40 Modern remote sensing instruments can provide continuous estimates of the boundary layer dynamics. Space-based remote sensing instruments, such as Moderate Resolution Imaging Spectroradiometer, Tropical Rainfall Measuring Mission data, and Multiangle Imaging SpectroRadiometer have also shown the ability to estimate PBL height (Wood and Bretherton 2004, Karlsson et al. 2010).

45 Ground-based lidar systems, such as the Raman lidars (Turner et al., 2014), ceilometer, micro pulse lidar (Campbell et al. 2002), atmospheric emitted radiance interferometer (Knuteson et al., 2004; Sawyer and Li, 2013), Doppler lidar (Tucker et al., 2009, Berg et al., 2017, **Bonin et al., 2018, Vakkari et al., 2015, Banakh et al., 2021**) and high spectral resolution lidar, have been commonly used to provide PBL height estimates (Quan et al., 2013, McNicholas and Turner 2014). For elastic lidar systems such as the micro pulse lidar,  $z_i$  is estimated by locating the height where the range-corrected signal-to-noise ratio (SNR) or attenuated backscatter profile experiences a strong decrease with height (Emeis et al., 2008). A similar approach is used to estimate  $z_i$  from profiles of water vapor mixing ratio from Raman lidar (Summa et al., 2013) or differential absorption lidar systems (Hennemuth and Lammert 2006); however, the peak in the water vapor variance has also been used as an estimate of  $z_i$  (Turner et al. 2014).

55 Doppler lidars provide range-resolved measurements of radial velocity, attenuated backscatter, and SNR. When staring vertically, a ground-based Doppler lidar measures height-resolved profiles of vertical velocity in the lower atmosphere with a temporal resolution of 1 second or less. Profiles of the vertical velocity variance can then be computed by averaging over an appropriate time interval (typically 15 to 30 minutes). The primary advantage of Doppler lidars is that they measure the turbulence directly and thus provide a more defensible measure of  $z_i$ . Other systems **rely** on gradients of aerosol loading or moisture that are used to infer  $z_i$ .

60 One method for estimating the convective boundary layer (CBL) depth **using Doppler lidars** is to find the height where the vertical velocity variance profile falls below some prescribed threshold, which in some cases can vary with time (Lenschow et al., 2000, Tucker et al., 2009, Lenschow et al., 2012, Berg et al., 2017). This method, which we refer to as the Tucker method, is simple to implement and provides a direct measure of  $z_i$ . However, the estimates are sensitive to the choice of variance threshold, which is somewhat arbitrary. Also, this method fails under stable nocturnal conditions due to weak

turbulence and the fact that the lowest gate of the lidar is often above the depth of the nocturnal  $z_i$ . Horizontal velocity variance and dissipation rate profiles from a Doppler lidar can be used to estimate  $z_i$  in nocturnal conditions (Vakkari et al., 2015, Banakh et al., 2021). Alternatively, one can estimate the PBL height based on wind shear and Turbulence Kinetic Energy (TKE), but there has been limited research on this topic (Brost and Wyngaard, 1978, Teixeira and Cheinet, 2004, Le Mone et al., 2018).

Due to different measurement approaches between multiple remote sensing instruments, considerable uncertainties exist when comparing  $z_i$  to standard radiosonde retrievals. PBL heights from different instruments provide expected trends during certain atmospheric conditions (mostly daytime convective time periods) but differ slightly due to measurement uncertainties and thresholds chosen associated with each instrument. Therefore, a framework independent of threshold techniques used in previous studies is warranted. Although this paper does not directly address a unified approach to estimate  $z_i$ , it is a step in that direction.

In view of these limitations, we investigate the potential of using a machine learning (ML) approach for continuous monitoring of  $z_i$ , with a focus on CBL. ML enables us to bring together various observations to arrive at a consensus answer. ML models, such as RF and Neural Networks, have been used for classifying various atmospheric phenomena (McGovern et al. 2017, Gagne II et al., 2019, Vassalo et al., 2020) or retrieving atmospheric variables (e.g., Solheim 1998, Cadeddu et al. 2009). The RF model is versatile, simple to implement, and robust. Training the RF model entails providing it with observations (i.e. features) that aid in predicting  $z_i$ . Examples of such observations include surface sensible and latent heat flux, soil temperature, soil moisture, surface potential temperature, surface humidity etc. These features have all been shown to exhibit some degree of correlation with  $z_i$  (Santanello et al., 2005; Zhang et al., 2013).

Here we use a RF model to predict  $z_i$  using input features derived from vertically-staring Doppler lidar data and various surface and sub-surface observations. We use a multi-year dataset from the U.S. Department of Energy (DOE)'s Southern Great Plains (SGP) site (Sisterson et al., 2016) for training and evaluating the RF model. Reference  $z_i$  measurements from radiosondes are used in the RF training process (Sivaraman et al., 2013). Specifically, the RF model is trained using observations from 2016 through 2018, and its performance is evaluated using data from 2019.

In this paper, Section 2 describes the observations that are used in this study, Section 3 describes the details of the RF model, including the training method, data conditioning and performance. Results of the RF model's performance are presented in Section 4, and in Section 5 we examine how RF model-derived  $z_i$  estimates affect the scaling of the vertical velocity variance profiles. PBL heights estimates from Energy Exascale Earth System Model (E3SM) Atmosphere Model version 1 (EAMv1), large-eddy simulations (LESs), and observations are compared in Section 6. Finally, a summary and future work are provided in Section 7.

The U.S. DOE Atmospheric Radiation Measurement (ARM) User Facility operates the SGP site in north-central Oklahoma (Mather and Voyles, 2013; Sisterson et al., 2016). The site contains an extensive suite of instrumentation for monitoring the atmosphere and surface properties. Most of these instruments operate continuously and the data are freely available from the ARM website (<https://adc.arm.gov/discovery>; McCord and Voyles 2016). The SGP site contains several heavily instrumented

100 subsites or “facilities” that are geographically dispersed over Oklahoma and Kansas (Mather and Voyles, 2013). For this study, we use observations from the central facility (C1), which also contains the largest number and most diverse suite of instruments in ARM. Figure 1 shows the layout of the SGP C1 site and the locations of instruments used in this study. Additionally, Table 1 lists the instruments, ARM data stream names, and specific measurements that were used. In ML,

105 the measurements from the observations will be referred to as features in the RF model.

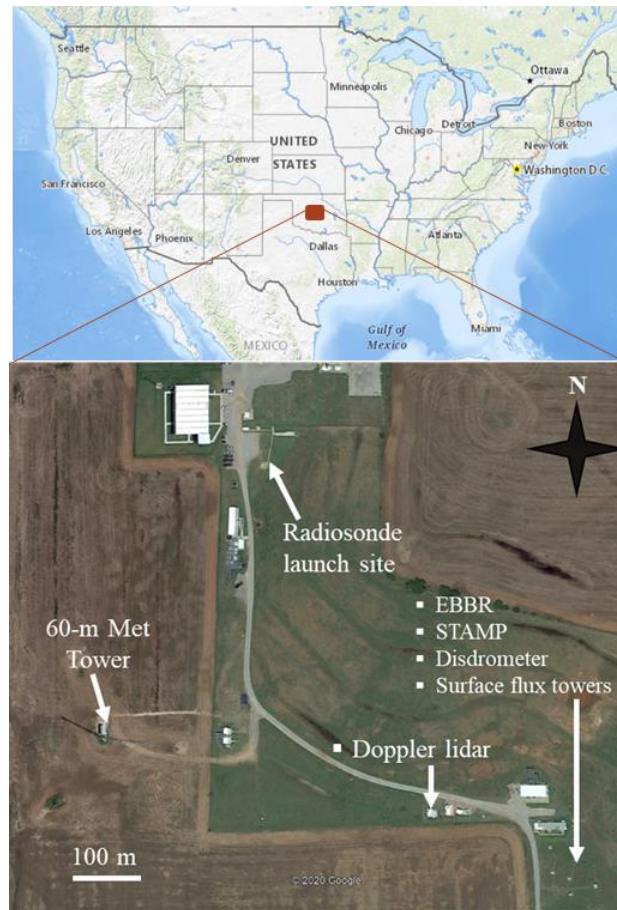


**Figure 1.** ARM SGP site C1 layout and instruments used in this study in Oklahoma, USA. Maps are extracted from © Google Earth and © Google Maps.

**Table 1: Instruments, ARM data stream names, and measurements used in this study.**

Instrument	ARM data stream	Measurements or features	Measurement height/range	References
Radiosonde	sgppblhtsonde1mcfar1C1.c1	PBL height estimates (m)	100 m to 5000 m AGL	Sivaraman et al., 2013
Surface eddy correlation station	sgp30co2flx25mC1.b1	Sensible heat flux ( $\text{Wm}^{-2}$ )	25 m AGL	Cook et al., 2018 and Tang et al., 2019
		Latent heat flux ( $\text{Wm}^{-2}$ )		
		Vertical velocity variance ( $\text{m}^2\text{s}^{-2}$ )		
		Friction velocity ( $\text{ms}^{-1}$ )		
		Turbulence Kinetic Energy ( $\text{m}^2\text{s}^{-2}$ )		
		Monin-Obukhov length (m)		
		Wind speed ( $\text{ms}^{-1}$ )		
		Wind direction (degrees from north)		
Surface meteorological station	sgpmetE13.b1	Air temperature (deg K)	4 m AGL	Ritsche and Prell, 2011
		Relative humidity (%)		
Soil temperature and moisture probes	sgpstampE13.b1	or Soil moisture ( $\text{m}^3\text{m}^{-3}$ )	-5 cm below surface	Cook, 2018
	sgpswatsE13.b1	Soil temperature (deg C)		
Surface energy balance system / solar infrared radiation station	sgpqcrad1longE13.c1 and sgpqcrad1longE13.c2	Best estimate of longwave, shortwave and normal radiation ( $\text{Wm}^{-2}$ )	2 m AGL	Cook and Sullivan, 2019
Doppler lidar	sgpdlfptC1.b1	Range-corrected attenuated backscatter variance ( $\text{m}^{-1}\text{sr}^{-1}$ ), SNR variance (dB), and average eddy dissipation rate ( $\text{m}^2\text{s}^{-3}$ ).	90 m to 800 m AGL	Champagne et al., 1977, Newsom and Krishnamurthy, 2020
	sgpdlprofwstats4newsC1.c1	Cloud base height (m) CBL depth from Tucker method (m) Year, month and hour of day	0 m to 9000 m AGL	Newsom et al., 2019b, Tucker et al., 2009
	sgpdlprofwinds4newsC1.c1	Wind shear exponent ( $\alpha = \log_{10}\left(\frac{U_1}{U_2}\right)/\log_{10}\left(\frac{Z_1}{Z_2}\right)$ ), where $U_i$ and $Z_i$ are wind speed and height at altitude $i$ .	$z_1 = 90$ m to $z_2 = 300$ m AGL (or lower, depending on data availability)	Wharton and Lundquist, 2012.

The ARM User Facility has operated a Halo Photonics Stream Line XR (Pearson et al., 2009) at C1 since April 2011. The instrument provides height- and time-resolved measurements of radial velocity, attenuated backscatter, and SNR. The range resolution is set to 30 m and the temporal resolution is about 1-s. The instrument is configured to stare vertically most of the time. Once every 15 minutes, it executes a plan-position-indicator scan, from which profiles of the wind speed and direction are computed. The vertical staring data are used to compute profiles of noise-corrected vertical velocity variance using a 30-minute averaging period. More details about the instrument are provided by Newsom and Krishnamurthy (2020). Details about the vertical velocity statistics value-added product (VAP) are provided by Newsom et al. (2019a), and detail about the Doppler lidar wind VAP are given by Newsom et al. (2019b).

Doppler lidar-derived features used in this study are listed in Table 1. The list includes raw height-resolved measurements of attenuated backscatter and range-corrected SNR, which are known to be directly correlated with  $z_i$  (Cohn and Angevine 2000, Brooks 2003). Also listed are several derived quantities such as cloud base height, wind shear, turbulence eddy dissipation rate, and  $z_i$  estimated using the Tucker method (Tucker et al., 2009). Typically, the nocturnal vertical velocity variance estimates are too small, and the threshold used in the Tucker method is not applicable. During certain rare nocturnal convection initiation events, larger vertical velocity variance estimates are observed and the same threshold ( $0.04 \text{ m}^2\text{s}^{-2}$ ) is used to estimate nighttime values of  $z_i$  from the lidar. For consistency in terminology being used here, we refer to all  $z_i$  estimates from the lidar as the Tucker method (both nighttime and daytime). Because the range of the Doppler lidars at SGP C1 is often less than 1 km (see Appendix A), estimates of eddy dissipation rate (using 1 Hz vertical velocity stares, Champagne et al., 1977) above 800 m were affected by system noise. Thus, features such as the eddy dissipation rate, attenuated backscatter, and SNR from the Doppler lidar were limited to 800 m AGL. Reducing the height from 800 m to 500 m AGL did not impact the results. Moreover, RF models used in this study are only capable of ingesting 1-dimensional timeseries data; therefore, 2-dimensional Doppler lidar features were averaged over the vertical column (90 m [lowest range gate] to 800 m AGL). Adding these features increased the overall variance explained by the RF model (82% of the total variance compared to 74% of the total variance without using lidar derived parameters).

The ARM PBL VAP (sgppblhtsonde1mcfar1C1.c1) contains estimates of  $z_i$  derived from radiosondes launched at SGP C1. We note that radiosondes are typically launched four times daily from SGP C1, nominally at 0530, 1130, 1730 and 2330 UTC each day (local time = UTC - 0600 hours). The PBL VAP uses three different algorithms for estimating  $z_i$ . These include the Heffter 1980, two bulk Richardson thresholds methods, and Liu and Liang (2010). The Heffter (1980) method is a well-established and widely used algorithm (e.g., Marsik et al. 1995, Delle Monache et al., 2004) that determines  $z_i$  from potential temperature gradients using criteria related to the strength of an inversion and the potential temperature difference across the inversion. The bulk Richardson number ( $Ri_b$ ) is a dimensionless number relating vertical stability to vertical shear. It represents the ratio of thermally produced turbulence to that generated by vertical shear. Methods using  $Ri_b$  to estimate  $z_i$  assume that there is no turbulence production at the top of the stable boundary layer and therefore  $Ri_b$  exceeds its critical value at the top of the boundary layer (Seibert et al., 2000). Several different critical thresholds of  $Ri_b$ , are provided in the literature

based on resolution of sondes, location, etc. The ARM PBL VAP includes  $z_i$  estimates based on two critical thresholds (0.25 and 0.5). Liu and Liang (2010) provide different thresholds for estimating convective and stable boundary layer depths using potential temperature profiles. The inversion strength thresholds used in the method varies for given stability regime and land type classification (land, ocean, or ice). We note that the various estimates can differ considerably. More details about the  
150 ARM PBL VAP are provided by Sivaraman et al. (2013).

## 2.1 Preliminary Data Analysis

Boundary-layer height estimation algorithms (Tucker et al., 2009, Berg et al., 2017, Bonin et al., 2018) purely using the Doppler lidars are limited by the range of the Doppler lidars at the ARM SGP facility, which may or may not reach the top  
155 of the boundary layer. The data availability of the ARM Doppler lidar SGP C1 systems is typically less than 1-2 km (Newsom and Krishnamurthy, 2020), and the data availability of the Doppler lidar vertical stares and velocity azimuth display scans for the study period are shown in Appendix A. The Tucker method  $z_i$  is used for inter-comparison with the RF model in this study, primarily due to its ease in application to the multi-year dataset, known performance, including its established usage in studies using the ARM Doppler lidar and other locations and instruments (Träumner et al., 2011, Shukla et al., 2014, Schween et al.,  
160 2014, Berg et al., 2017, Lareau et al., 2018, Lareau 2020). Vertical velocity variance profiles provided in the `sgpdlprofwstats4newsC1.c1 VAP` and a variance threshold of  $0.04 \text{ m}^2\text{s}^{-2}$  is used to determine  $z_i$ , following Tucker et al., 2009. The results are somewhat sensitive to the choice of threshold such that the  $z_i$  estimates decrease as the threshold is increased (Berg et al., 2017).

Figure 2 shows a typical example of vertical velocity variance during the warm season at SGP. Also shown are  
165 estimates of  $z_i$  from the Tucker method. We find that the Tucker method generally works well at tracking the height of the convective mixed layer during its initial development phase and can be made to match the radiosonde observations by changing the vertical velocity variance threshold (Schween et al., 2014). In that case, there is sufficient SNR for the lidar to see both the developing convection and the overlying residual layer. However, as the mixed layer continues to deepen, at some point the SNR becomes too small to enable reliable estimates of the vertical velocity variance. This problem is sometimes  
170 compounded by a slight reduction in sensitivity during the hottest portion of the day, which we suspect is the result of strong refractive turbulence in the surface layer. Although this effect has not been thoroughly analysed due to lack of refractive turbulence profiles and concurrent radiosonde data, there could be instances when the Doppler lidar is indeed measuring the top of the boundary layer. In any event, the loss of signal near the CBL top could result in  $z_i$  estimates from the Tucker method to be low biased.

175



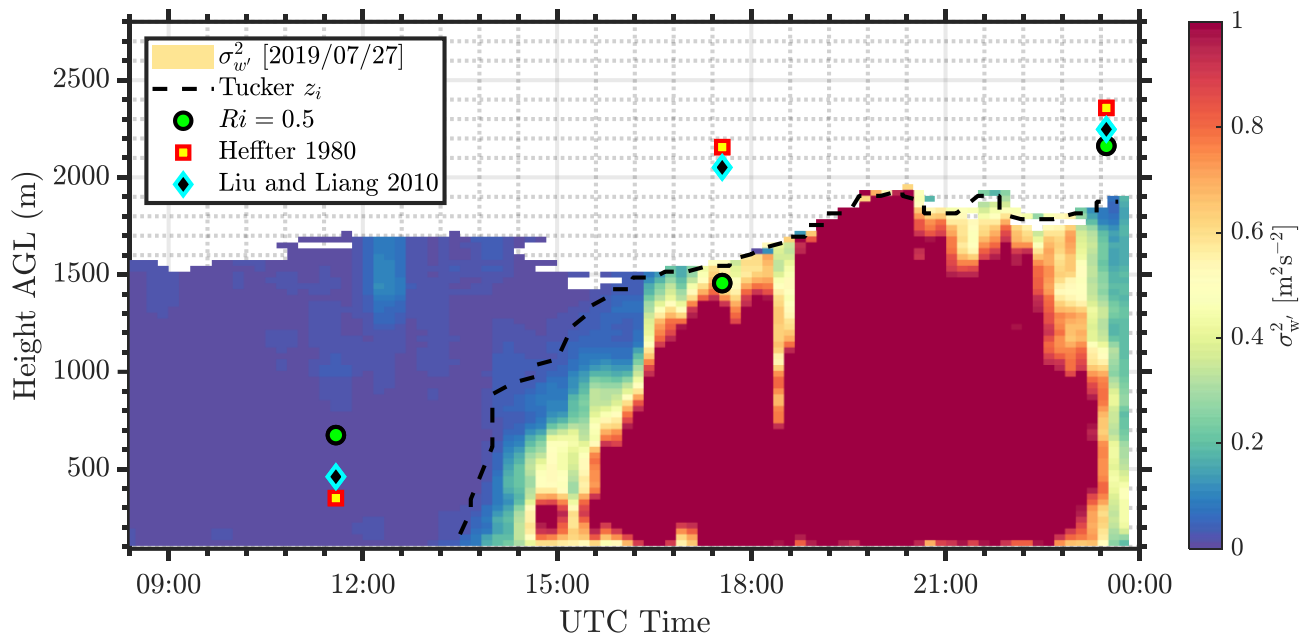


**Figure 2: Typical CBL showing lidar variance (colours), Tucker  $z_i$  (black line), and radiosonde  $z_i$  (three methods; symbols). The horizontal axis shows the number of hours after 00:00 UTC on 27 July 2019.**

180 For this study, radiosonde-derived  $z_i$  estimates are used to calibrate the RF algorithm. Figure 3 shows comparisons between lidar-derived CBL (using the Tucker method) and simultaneous estimates from the ARM PBL VAP. These comparisons were performed using 1785 cases with radiosonde data and daytime clear (identified as periods when surface heat flux is positive from sunrise to sunset and cloud base height is zero) or shallow cumulus conditions (identified as cloud base height less than 5 km from Doppler lidar and cloud fraction less than 0.1) for the years 2016 through 2019. From these results,

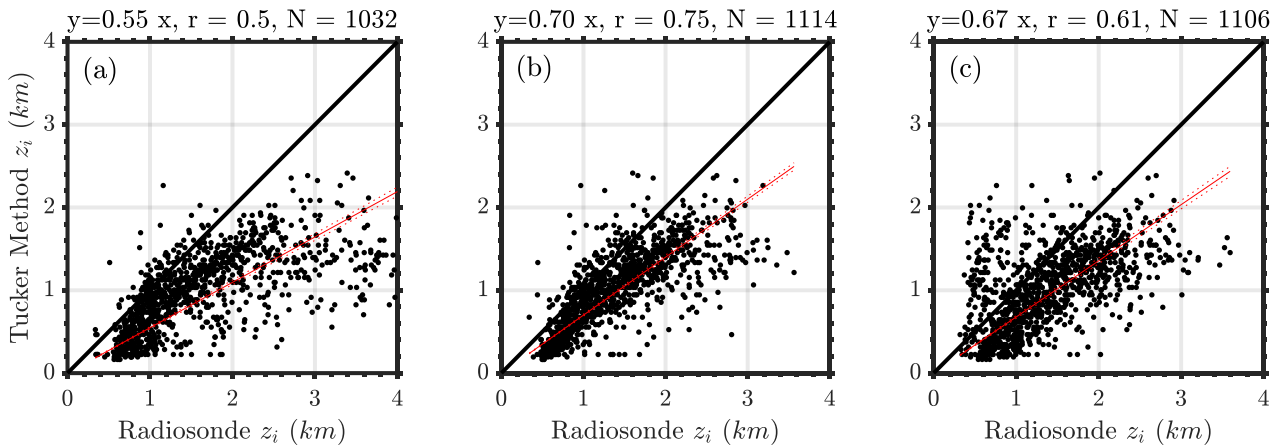
185 we found that the Liu and Liang (2010) technique resulted in the best overall agreement with the Tucker method  $z_i$ , in terms of the correlation coefficients ( $r = 0.75$ ) and slope (0.70). Thus,  $z_i$  estimates from the Liu-Liang technique in the ARM PBL VAP (pblhtsonde1mcfar1.c) are used as a reference to calibrate the RF model in this study. It should be noted that any of the above three model outputs can be used to calibrate the ML model, if needed, and the choice could vary with each site. For a different site, we would recommend conducting a similar correlation analysis as shown above with various radiosonde models

190 and lidar data to determine the optimal model for RF calibration. It is important to note that during stable conditions, the determination of  $z_i$  from radiosondes is very uncertain, as the turbulence can result from either buoyancy forcing or wind shear and radiosonde rapidly rises through the relatively thin stable boundary layer. At SGP C1, the nose of the low-level jet can also be used to define the height of the boundary layer (Sivaraman et al., 2013). Therefore, the focus of this study is to only demonstrate the ability of the RF model to replicate nighttime  $z_i$  estimates compared to radiosonde-derived values. We hope

195 this framework developed in this article can be adapted easily to future research in estimating the true stable boundary layer



height from radiosondes or other reference sources. During stable conditions, the true  $z_i$  can be below the lowest range-gate of the Doppler lidar and we expect such a technique would aid in representing true  $z_i$ , estimates with proper calibration.



200 **Figure 3: Comparisons between Tucker method and three different  $z_i$  estimates from radiosondes a) Heffter 1986, b) Liu and Liang 2010 and c) Bulk Richardson number method using a threshold of 0.5. The red line is the best fit with the fit  $y = mx$  shown above.  $r$  is the correlation coefficient and  $N$  is the total number of radiosonde and Tucker method observations used in each scatter plot.**

### 3 Machine Learning

205 In this study, an RF algorithm was used to predict PBL heights. RF regression (Breiman, 2001) is an ensemble method that is made up of a population of decision or decorrelated trees. Figure 4 provides a graphical illustration of the RF bootstrapping process. Bootstrap aggregation (bagging) is used so that each RF tree (a sample is shown in Appendix B) can randomly sample from an entire feature set, while only a subset of the total feature set is given to each individual tree. For example, if the entire feature set contains say  $M$  different features, an individual RF tree can contain a fraction of those  $M$  features. The premise behind RF is to improve the variance reduction of bagging by reducing the correlation between the trees without increasing the variance. The trees can be truncated to add further diversification. After construction, the population's individual predictions are averaged to give a final prediction of the target variable. Ideally, this process results in a diversified and decorrelated set of trees whose predictive errors cancel out, producing a more robust final prediction.

215 An advantage of RFs is their ability to determine the importance of all input features for the predictive process. This is done by calculating the mean decrease in impurity, or the decrease in variance that is achieved during a given split in each decision tree. The decrease in impurity for each input feature can be averaged over the entire forest, providing an approximation of the feature's importance for the prediction (feature importance estimates sum to 100% to ease interpretability). A sample regression tree developed by real data used in this article is shown in Appendix B (Figure B1). The statistics and ML toolbox in MATLAB contain all the functions needed to build the RF algorithm used in this study.

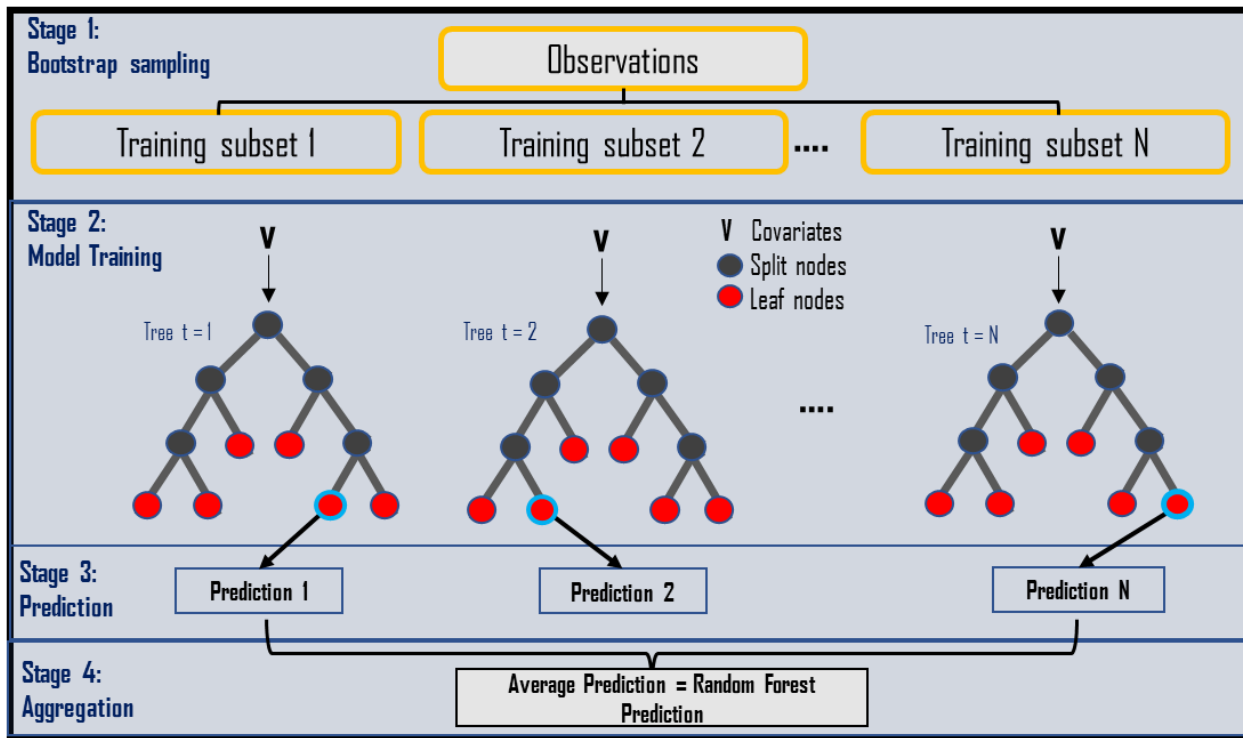


Figure 4: Graphical representation of a standard RF algorithm (adapted from online sources and Figure A1).

### 3.1 Model Hyperparameters

225 In this study, a least-squares boosting regression (LSboost) ensemble RF model (Breiman 2001) is built based on observational data listed in Table 1. At every iteration, the ensemble fits a new decision tree to minimize the mean-squared error between the observed response and the aggregated prediction of all decision trees developed previously. The MATLAB function *fitensemble* is used to develop the RF model. The algorithm creates several regression trees using a subset of input features and radiosonde observations. The RF model creates a learning process to map the reference data to input features.

230 Hyperparameters are used to control the learning process in the RF model. It is good practice to tune hyperparameters such as the maximum number of decision splits per tree (see Figure 4), learn rate for shrinkage and the number of iterations for reducing the generalization error (Breiman, 2001). In this article, hyperparameters for the RF model are chosen by performing a Bayesian optimization on the data, which minimizes the k-fold cross validation loss function for select hyperparameters (MATLAB function *bayesopt*). For this study, three hyperparameters were optimized: the number of tree splits, number of

235 learning cycles or iterations, and learn rate for the model. Based on the optimization results, the number of iterations was set to 460, number of tree splits to 11 and the learning rate was set to 0.25 for the current model.

Regularization techniques are used to prevent statistical overfitting in a predictive model (Hastie et al., 2008), by reducing the magnitude of the coefficients of the RF model for certain parameters that do not contribute to the target variable. In general, regularization algorithms can treat issues such as multicollinearity and redundant predictors and make the model more precise. The MATLAB function *regularize* is used for the regularization process, which is based on the Lasso regularization algorithm (Tibshirani, 1996). This regularization algorithm optimizes the number of trees and avoids data overfitting.

### 3.2 Data Preprocessing

Surface and lidar data from 2016 to 2019 are used in this analysis. ARM VAPs provides processed and quality-controlled data from several atmospheric sensors. Each VAP provides quality control thresholds that are used to filter the data. For example, the lidar VAPs (DLWSTATS and DLWIND) provide quality control flags based on the system noise and SNR (Newsom and Krishnamurthy, 2020). For this analysis, thresholds specified in the VAPs are used to remove any erroneous data. Similarly, quality control flags for all variables mentioned in Table 1 above are used to filter bad data (Tang et al., 2019). Because the temporal resolution of the surface data are variable, measurements are interpolated or averaged to the lidar 15-minute resolution time stamps. The frequency of radiosondes is generally 6 hours at SGP but can be in intervals of 3 hours during select field campaigns (Mather et al., 2018). For training purposes, surface and lidar data to the nearest radiosonde observations within 15-minutes are chosen.

Normalizing/standardizing/scaling processes are used to scale the variables in an ML model, such that they have the same order of magnitude in their value. Standardizing involves aligning the features to have a zero mean and scaled to have standard deviation of one. Typically, RF models do not need standardizing or normalizing features due to the inherent bagging process (Breiman, 2001). At SGP C1, large diurnal variability was observed for certain parameters (like TKE, dissipation rate, etc.), leading to a large distribution of values between daytime and nighttime. This skewed the number of trees the RF model builds for daytime and nighttime estimates. Standardizing the features showed improvements while estimating nocturnal  $z_i$  estimates from the RF model. Therefore, to improve nocturnal  $z_i$  estimates, standardized datasets will be used in the following analysis for all conditions.

All the features, listed in Table 1, are filtered based on ARM mentor guidelines for each instrument and then normalized. These measurements are fed into an ensemble RF model using the hyperparameters described above. Once the RF model is built, a Lasso regularization approach is used on the RF model to limit the effect of collinearity on the target variable. Similar to a least-squares regression, collinear columns tend to deteriorate the accuracy of the output (Krishnamurthy et al., 2013, Yoo et al., 2014). Once the RF model is built, it can be used to estimate  $z_i$  for time periods that are not being used to train the model. In MATLAB, this is typically done using the *predict* function.

The RF model is trained using sub-surface, surface, lidar and concurrent radiosonde  $z_i$  data from 2016, 2017 and 2018. Hereon, these data are referred to as training-input features. A total of 3919 radiosonde  $z_i$  measurements were used in the training process. The 2019 sub-surface, surface and lidar data are referred to as future-input features and are used to provide

270 an independent dataset to evaluate the trained RF method. From an operational perspective, missing input features are quite common. The most common approach is to fill in (impute) the missing features (Hastie et al., 2008). Surrogate data using a local median of the nearest 10 data points are used in the analysis (Hastie et al., 2008). Other imputation algorithms such as k-nearest neighbour was also tested, and similar results were observed. It is critical for the RF model to deal with missing values in its training phase. In some cases, the added noise in the system can help improve the stability of the RF model. But too much noise is also detrimental in the training process, and the imputed data may no longer be useful and can cause erroneous results. The imputation process is done inherently during the RF bagging process. The effect of data imputation on model performance was evaluated by training the RF model with and without data imputation. Four different possibilities in evaluating the performance of the RF model with and without imputation are evaluated, as shown in Table 2 below. In the case of no imputation (no missing data), only time periods when all features/parameters are available are used in the RF regression. In the case of 50% missing data, approximately 50% of the time series data were missing (at random) due to say issues with data quality and surrogate data were used. The choice of 50% was to mimic a worst-case real-world scenario based on experience, where either one or two instruments from the feature set of 20 odd variables have data quality issues. Other combinations, such as no missing data used in the RF regression during training process and 50% future-input feature missing data and vice versa were evaluated.

285

**Table 2. Data imputation evaluation and performance on boundary layer heights for year 2019**

Case	Training-Input Features	Future-Input Features	R <sup>2</sup> (%)	RMSE (m)	$Y_{RF} = m X_{RS} + C$
No Imputation	No missing data	No missing data	76.86%	324	$Y_{RF} = 0.912 X_{RS} + 211$
Future-Input Imputation	No missing data	50% missing data imputed	65.28%	366	$Y_{RF} = 0.789 X_{RS} + 288$
Training-Input Imputation	50% missing data imputed	No missing data	76.15%	328	$Y_{RF} = 0.876 X_{RS} + 258$
Training and Future-Input Imputation	50% missing data imputed	50% missing data imputed	66.50%	357	$Y_{RF} = 0.792 X_{RS} + 324$

\* RF – Random forest, RS – Radiosondes

290 As can be seen from Table 2, data imputation overall reduces the accuracy of RF model performance. Missing future-input features seems to have the highest effect on the RF model  $z_i$  estimates, regardless of training the model based on missing training-input features. This could be due to several reasons, such as the median value does not represent the current state of the missing data, the same input features are not missing in both training and future input features as the combinations to test are near infinite (as the data in real-world can be missing in random as in the case above), etc. Assessing the performance of the RF algorithm using data imputation creates an additional level of complexity when one of the features is missing for a given time step compared to others. For example, if relative humidity feature is missing for a given time step and lidar

295

measurements are missing for another time step, the effect on the RF model output is not similar. The RF model provides weights to each feature, and the impact on the RF model would be dependent on the calibration and ability of the imputation algorithm to estimate the missing value. Since there are several possible scenarios here (as we have close to 20 odd features), and capturing all errors effectively would be a challenge, as each feature is not weighted equally in the model. Therefore, in this analysis, the model is trained with no missing data, and no imputation is done on the data (either input or future features) to accurately test the efficacy of the RF model. The authors would like to note that the results in Section 4 are in some sense optimistic due to the treatment of missing data, and the worst-case performance of such an algorithm must be thoroughly evaluated. Future studies are planned to implement a better imputation model based on data from past trends for a given feature and to test RF model performance.

RF models are generally site specific; initial tests (not shown) show the possibility to develop a generalized RF model to estimate  $z_i$  for all sites around SGP (C1 and other satellite sites) with good accuracy under all atmospheric conditions. A round-robin type analysis, where a model developed at a given site is tested at every other site and vice versa, would be a valuable exercise (Bodini and Optis, 2020).

#### 4 Performance of RF $z_i$

Boundary layer height predictions from the RF model and Tucker method were compared to radiosonde estimates. Mean absolute error (MAE) is defined as:

$$MAE = \frac{1}{N} \sum_{i=1}^N |z_{iRS} - z_{iY}| \quad (1)$$

Where,  $z_{iRS}$  is the boundary layer height estimated from the radiosondes (Liu and Liang, 2010),  $z_{iY}$  is the boundary layer height estimated from either the Tucker method or RF model. The root mean square error (RMSE) is defined as

$$RMSE = \sqrt{\frac{1}{N} \sum_{i=1}^N (z_{iRS} - z_{iY})^2} \quad (2)$$

Similarly, the linear correlation coefficient ( $R$ ) is defined as

$$R = \frac{1}{\sigma_{RS}\sigma_Y(N-1)} \sum_{i=1}^N (z_{iRS} - z_{RS})(z_{iY} - z_Y) \quad (3)$$

325 Where,  $z_{RS}$  and  $z_{\gamma}$  denote the mean of radiosonde and RF/Tucker method boundary layer heights, respectively,  $\sigma_{RS}$  and  $\sigma_{\gamma}$  denote their standard deviations, and  $N$  denotes the number of samples.

MAE and RMSE for the daytime atmospheric conditions from Tucker and RF methods are shown in Table 3. Daytime is defined as the period when surface heat flux is positive (i.e., sunrise to sunset), clear sky is defined as time periods when no clouds are observed from the Doppler lidar (with an hourly cloud fraction less than 0.1) and cloudy conditions are defined as  
 330 time periods when clouds below 5 km are observed from the Doppler lidar (with an hourly cloud fraction greater than 0.1). It can be observed that the RF method shows considerable improvements compared to the Tucker method for all three categories. Improvements of 40-50% in MAE and RMSE are observed under various conditions. The least improvement in RF  $z_i$  estimates is observed during cloudy conditions, with a MAE improvement of 45% compared to the Tucker method. Correlation coefficients are also observed to improve significantly during all daytime conditions.

335 Due to the presence of a nocturnal low-level jet (LLJ) at SGP, all seasons, the radiosonde nighttime  $z_i$  estimates are generally below the LLJ height and are well tracked by the RF model (see Section 4.1). A comparison of nocturnal RF model  $z_i$  estimates with other remote sensing devices that continuously monitor the boundary layer height needs to be conducted (e.g., Raman lidar) and is a part of future work.

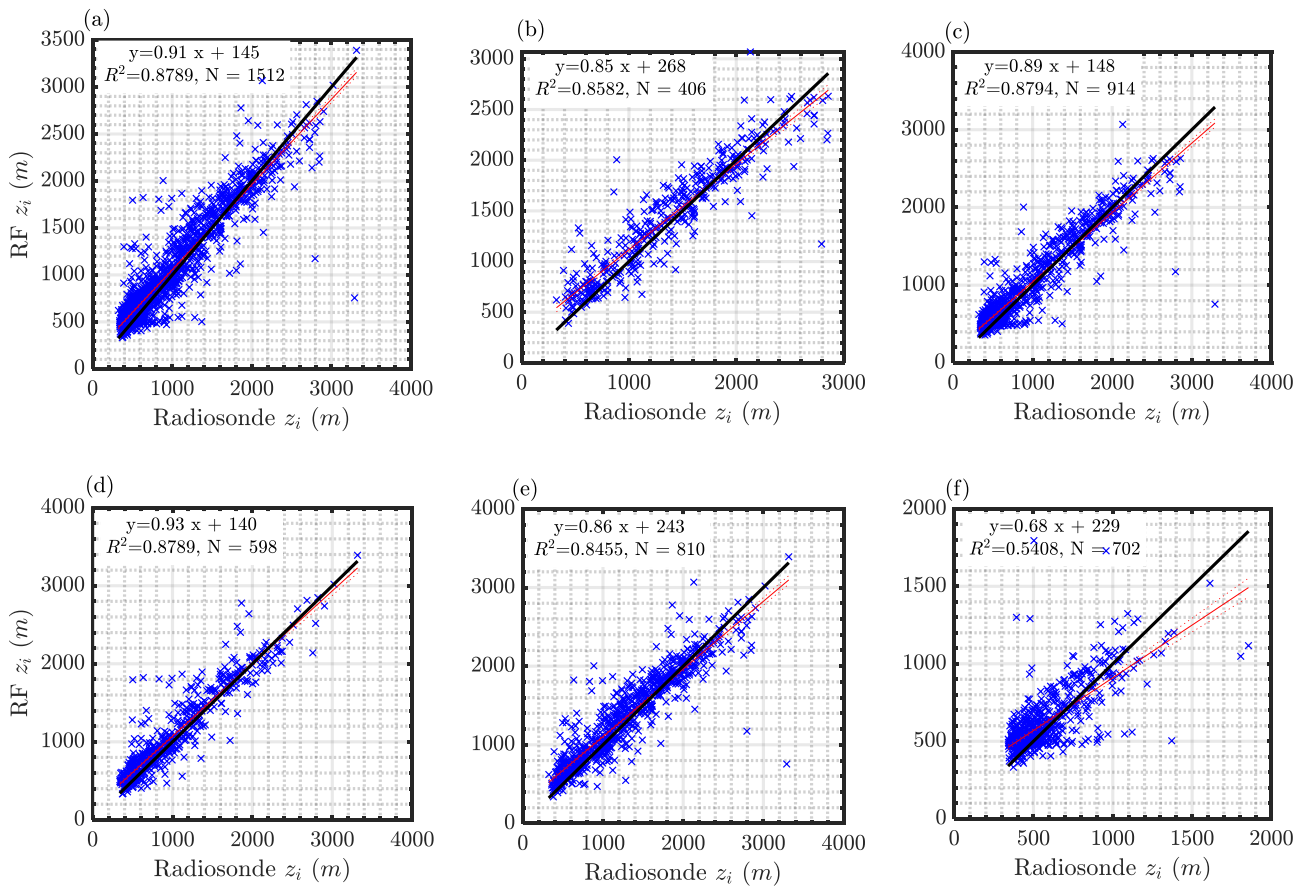
340 **Table 3. Systematic mean absolute errors, root mean square error and correlation coefficient ( $R^2$ ) between RF, Tucker method, and radiosonde  $z_i$  estimates in 2019.**

Observed atmospheric conditions	MAE (m)			RMSE (m)			$R^2$	
	RF	Tucker Method	% Improvement	RF	Tucker Method	% Improvement	RF	Tucker Method
Daytime Only	167	311	46%	249	441	43%	0.845	0.545
Daytime Clear sky	165	336	51%	235	479	51%	0.857	0.520
Daytime Cloudy	141	255	45%	208	363	43%	0.878	0.725

Nocturnal estimates of  $z_i$  from radiosondes at SGP are much more uncertain (Sivaraman et al., 2013). Regardless of the accuracy of the  $z_i$  estimate from radiosondes, the ability of the RF model to predict the input data is evaluated.  
 345 Consequently, the data were split into five atmospheric conditions: 1) daytime and clear sky (26%), 2) day and night clear sky (60%), 3) day and night cloudy (40%), 4) daytime only (53%), and 5) nighttime only (46%). Although some cases overlap in the above situations, the idea was to evaluate the RF model performance reasonably during both daytime, nighttime, cloudy, and clear-sky condition combinations. These five atmospheric conditions were chosen, because these are commonly observed atmospheric conditions at SGP and have been observed to have an impact on  $z_i$  (e.g., variations in cloud base height varies  $z_i$ ).  
 350 The associated correlation plots between RF  $z_i$  estimates and corresponding radiosonde  $z_i$  estimates are shown in Figure 5. Overall, the RF model  $z_i$  estimates correlate well with radiosonde  $z_i$ , with an  $R^2$  of greater than 0.85 during all the above conditions. During clear sky conditions (including both daytime and nighttime), RF  $z_i$  estimates show the highest correlation

of 0.88. Although the sample size varied for five categories, the correlation coefficients are overall high for the RF  $z_i$  estimates (compared to Tucker method in Figure 3). During the night, the  $z_i$  values from the radiosondes are relatively constant, and the RF estimates are consistent with these values. However, due to the small dynamic range of the nighttime  $z_i$  values, the correlation between the radiosonde and RF methods is relatively poor (0.54). Based on the slopes of the regression lines in Figure 5, the RF model tends to overestimate  $z_i$  when it is small and slightly underestimate  $z_i$  when it is large. Possible reasons for this trend are under further investigation.

Overall, a uniform improvement in  $z_i$  can be obtained using RF techniques. Reducing or increasing the training data had an impact on the RF model performance, but the increase in the magnitude of the correlation coefficient was negligible using at least two years of data. In this analysis, three years of data were used for training the RF model.

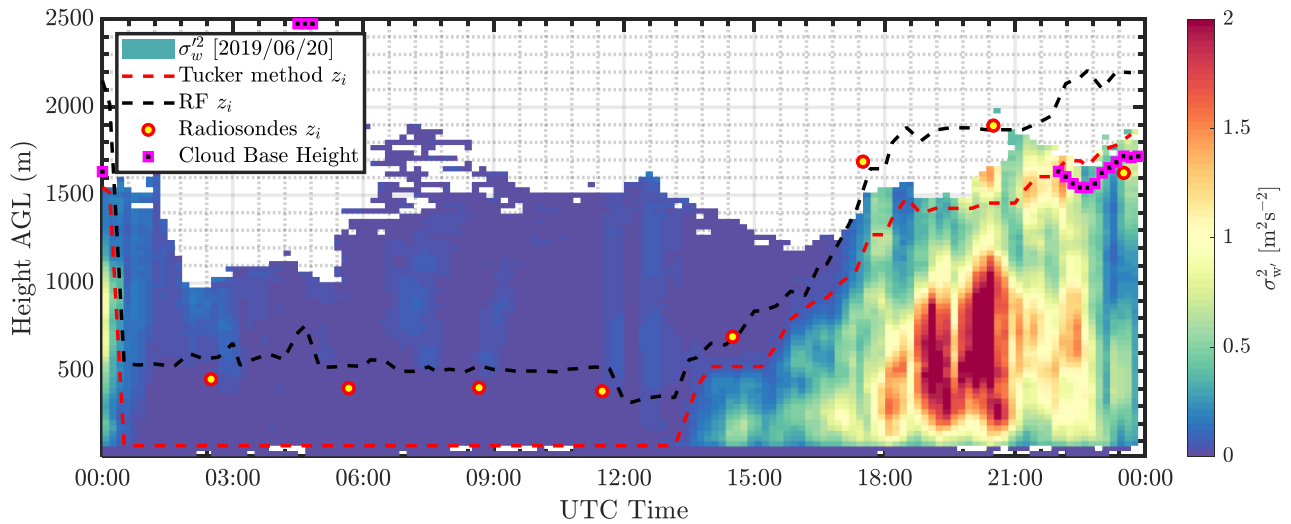


365 **Figure 5: Correlations between RF PBL height and radiosonde PBL height for a) all data in 2019, b) daytime clear sky, c) clear sky daytime and nighttime, d) cloudy daytime and nighttime, e) daytime only, and f) nighttime only.**



#### 4.1 Time series, diurnal, and seasonal performance

The RF model was trained using data from 2016 to 2018, and  $z_i$  estimates for 2019 were estimated using the parameters listed in Table 1. **The temporal resolution of the RF model  $z_i$  estimates is 15 minutes.** Figure 6 and Figure 7 show lidar  $z_i$  estimates from **the** Tucker method, radiosondes and RF model on June 20 and June 22, 2019, respectively. Cloud base height and vertical velocity variance profiles from Doppler lidar are also overlaid. Due to an ongoing field campaign, the micropulse differential absorption lidar demonstration project, these days observed a higher frequency of radiosonde observations (Weckwerth et al., 2020). It is clear **that** the RF model  $z_i$  closely follows radiosonde  $z_i$  estimates and the Tucker method underestimates  $z_i$  as estimated from radiosondes. Although, the Tucker method is observed to track the convective boundary layer height effectively, a bias is observed when compared to the radiosonde  $z_i$ . Optimizing the vertical velocity variance thresholds could potentially reduce the bias in certain conditions, but the bias is not uniform across all time periods (see Figure 7). **Because** aerosol concentration decreases with altitude, signal availability reduces as a function of height. During peak convection, when the aerosol concentration above the boundary layer is minimal, lidar measurements sometimes do not reach the top of the boundary layer with sufficient SNR to be detected. The lidar beam also attenuates considerably when it encounters clouds or fog due to increased atmospheric scattering or attenuation. In Figure 6, it can also be seen that lack of aerosols limits the Doppler lidars' ability to measure above the boundary layer height during peak convective periods. During nighttime conditions, vertical velocity variance is low and is not effective in estimating  $z_i$ . In this study, the lowest range-gate is used as the stable boundary layer height from the lidar as a first guess. As mentioned earlier, nocturnal conditions during summer months are dominated by southerly winds where in the nocturnal boundary layer is capped by a low-level jet (Krishnamurthy et al., 2020). During these conditions, the RF model shows near constant  $z_i$  which is observed to be well correlated with radiosonde  $z_i$  (just below the LLJ height).



390

**Figure 6: Boundary layer height estimates at the SGP central facility on June 20, 2019 from Tucker method (Tucker et al., 2009), RF model  $z_i$ , radiosondes  $z_i$  (Sivaraman et al., 2013), cloud base height estimates from lidar (Newsom et al., 2019), and the background colours represent vertical velocity variance measurements from Doppler lidar.**

395

In Figure 7, the effectiveness of the RF model can clearly be observed. At 0300 hours and 0600 hours UTC, during stable nocturnal conditions, the RF model matches the radiosonde estimates very well. At 0900 hours UTC, a possible nocturnal convection initiation event results in high vertical velocity variance for several hours (Reif et al., 2017). Convection initiation refers to the process in which an air parcel is successfully lifted to its level of free convection and produces a precipitating updraft (Markowski and Richardson, 2010). The RF model is observed to detect that burst of convection and provide coherent boundary layer heights past 1200 UTC until daytime transition at ~1400 UTC. The correlation between RF model and radiosonde  $z_i$  estimates is very high. Therefore, various atmospheric interaction effects are aptly characterized by the parameters in the RF model. Hourly averaged  $z_i$  and daily maximum  $z_i$  averaged for each season in 2019 from Tucker method, RF model, and radiosondes are shown in Figure 8a. Although, the number of samples between the radiosondes and RF model estimates are vastly different, the generic trend in the hourly and seasonal boundary layer height variability is well captured by the RF model. Although the Tucker method captures the average boundary layer height trend, it shows a clear bias in convective boundary layer height estimates compared to radiosonde and RF model derived  $z_i$  values. As observed earlier from the time series analysis, a standard bias correction would not always improve  $z_i$  estimates from the Tucker method. Daily daytime maximum  $z_i$  estimates averaged over four seasons in 2019 from all three methods are shown in Figure 8b. Summer months (May through August) show high boundary layer heights. During these months, the peak convective period occurs during the daytime at around 2000 hours UTC, and the average boundary layer height as observed from the RF model is ~2100 m above ground level, which correlates well with radiosondes released during the same time period. During winter and fall months, the peak convective period does not always occur at 2000 hours UTC and therefore the maximum  $z_i$  estimates

405

410

from radiosondes do not coincide with RF estimates. The Tucker method invariably underestimates maximum  $z_i$  during all seasons.

415

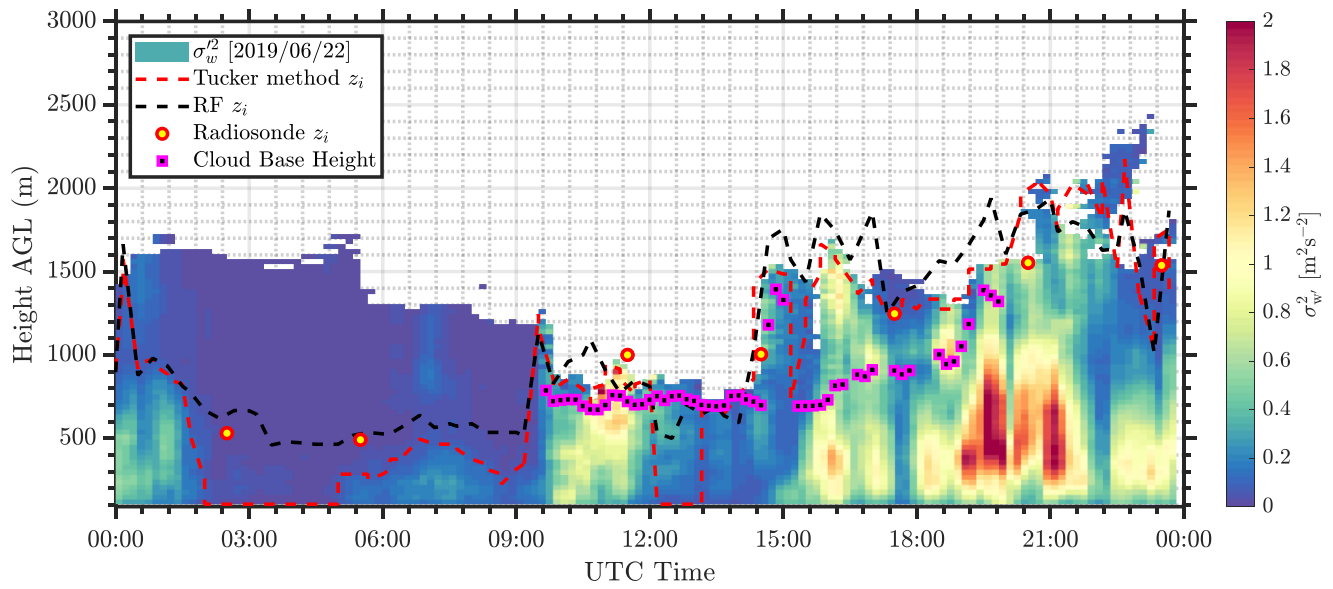
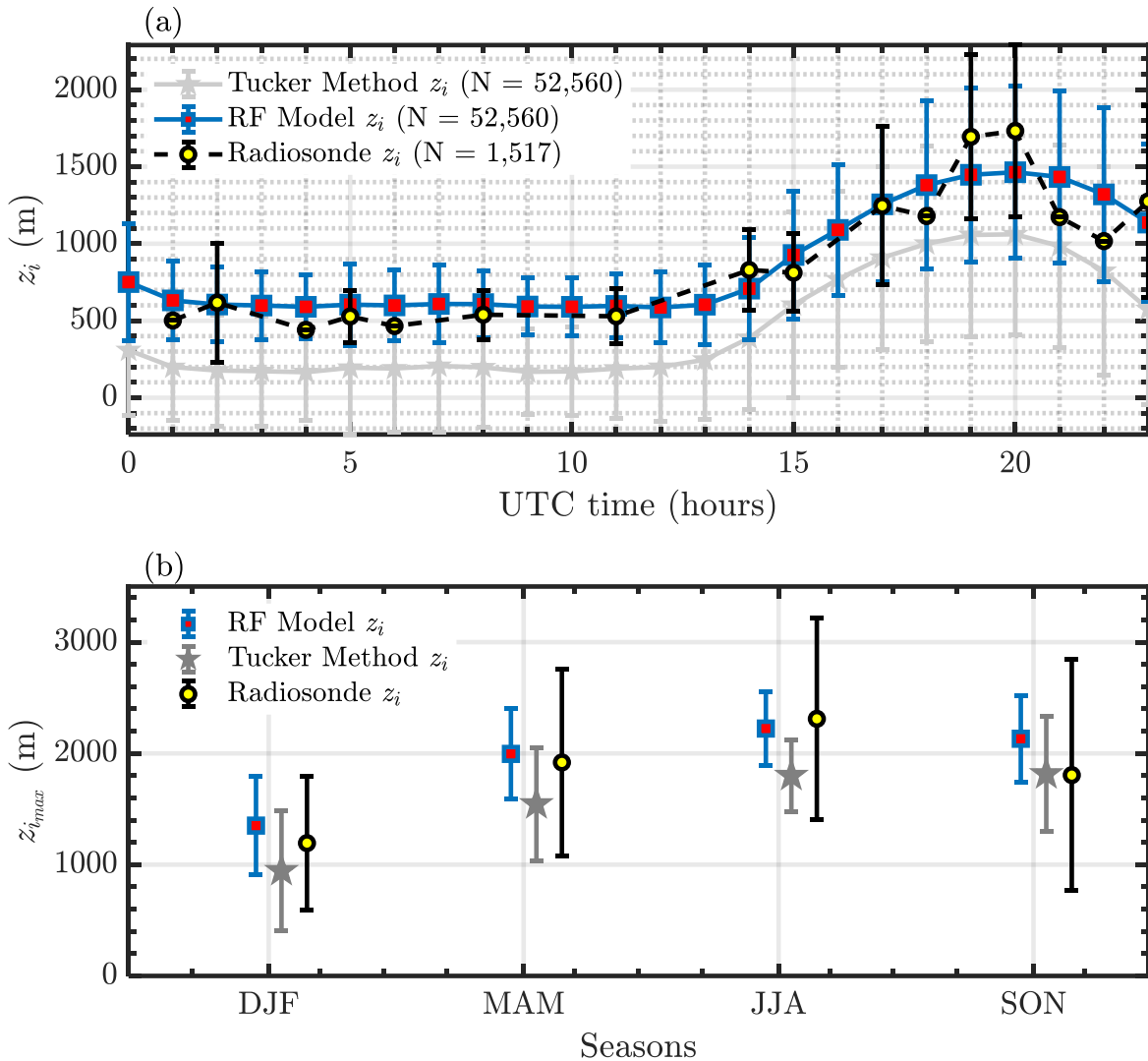


Figure 7: As in Fig. 6, but for June 22, 2019.



420 **Figure 8:** a) Hourly averaged  $z_i$  estimates at SGP central facility for 2019 from RF, Tucker method, and radiosondes. Total number of samples (N) for each dataset is also shown in the legend. b) Daily daytime maximum  $z_i$  estimates for four seasons (DJF, MAM, JJA, SON) from RF, radiosonde, and Tucker method. The bars in both plots represent one standard deviation.

## 4.2 Input Feature Importance

425 All the input features within the RF model explain approximately 82% of the total variance in the data. Table 4 provides the unbiased predictor importance estimates, which is computed by permuting or shuffling a variable in the model and estimating its mean square error (Breiman, 2001). If a predictor is significant in prediction, then permuting its values will affect the model error and vice versa. However, if two input variables are highly correlated (as is expected when testing

atmospheric forcing), it is highly unlikely that the reported importance values will accurately represent each variable's  
 430 significance (Breiman, 2001). Based on this analysis, the most important parameter is the initial  $z_i$  guess from the Tucker  
 method. This provides a very good first guess to the RF model, especially during convective conditions. Although the RF  
 model is sensitive to the initial guess from the Tucker method, it is observed to be robust enough to ignore uneven spikes in  $z_i$   
 estimates due to noise in the lidar vertical velocity variance data (Figure 7). The second most important feature observed to  
 have high correlation with  $z_i$  estimate is the hour of the day. A clear diurnal pattern in  $z_i$ , i.e., higher values in the daytime and  
 435 near constant values during the nighttime, estimates are observed at SGP. Therefore, hour of the day can effectively classify  
 the data, which is beneficial in the RF bagging process. Relative humidity also shows higher importance ( $> 5\%$ ), where drier  
 conditions are observed to have higher correlations with boundary layer height. Deep convection and larger  $z_i$  is generally a  
 consequence of greater sensible heat flux and lower latent heat flux, which are primarily due to higher surface temperature and  
 lower relative humidity. Based on an evaluation of  $z_i$  over Europe, it was also observed that relative humidity had a strong  
 440 negative correlation with  $z_i$ , and surface temperature had a positive correlation (Zhang et al., 2013). Other features such as  
 lidar attenuated backscatter, surface air temperature, Monin-Obukhov length, soil temperature, surface wind direction, and  
 TKE all are observed to be important for accurately characterizing the boundary layer height at SGP. Other surface features  
 such as surface friction velocity, sensible heat flux, longwave radiation, etc., have lower correlations with  $z_i$  within the RF  
 model framework. Therefore, the model can be reduced to the list of parameters defined in Table 4 for optimal estimation of  
 445 the boundary layer height at SGP.

**Table 4: Key parameter/feature unbiased importance estimates during all conditions**

Parameters/Features	% Importance
Tucker method $z_i$	58.67%
Hour of the day	10.05%
Surface Relative Humidity	6.82%
Attenuated Backscatter	2.90%
Surface Air Temperature	2.77%
Monin-Obukhov Length	2.77%
Soil Temperature	1.92%
Surface Wind Direction	1.78%
Turbulence Kinetic Energy	1.32%
Others	$< 11\%$

To assess the key features during nighttime, a similar RF model was built by conditionally sampling nighttime data.  
 450 During nighttime, the key parameters that affect the RF model predictions are shown in Table 5. It is interesting to note that  
 the key features deemed important during nighttime are significantly different compared to all conditions, and the percent  
 importance is more evenly distributed across many features. This result alludes to the fact that nocturnal stable boundary  
 layers are indeed complex to model and several processes are at play (Fernando and Weil, 2010). Monin-Obukhov length is

observed to have the highest impact on the nighttime RF model estimates and is consistent with theory on stable boundary  
 455 layers (Zilitinkevich, 1972, Zilitinkevich and Baklanov, 2002). Although nighttime  $z_i$  initial guesses are generally a constant  
 (lowest lidar range-gate if no high vertical velocity variance is observed), the initial guess has shown to be effective in adjusting  
 the RF model  $z_i$  estimates. Other local parameters such as soil temperature, surface air temperature, dew point temperature,  
 longwave radiation and turbulence kinetic energy are observed to be correlated with nighttime  $z_i$  estimates. One of the stable  
 boundary layer models by Brost and Wyngaard 1978 is given by:

460

$$z_i = 0.4 \left( \frac{u_* L}{|f|} \right)^{1/2} \quad (4)$$

Where  $u_*$  is the friction velocity,  $L$  is the Monin-Obukhov length, and  $f$  is the Coriolis parameter. As shown in Table 5, the  
 nighttime parameters deemed important by the RF model include both Monin-Obukhov length and friction velocity. As  
 465 discussed earlier, the dominant feature of nocturnal boundary layer at SGP is the presence of the LLJ. The turbulence  
 production at SGP is not only influenced by surface characteristics but also heavily influenced by the presence of the LLJ. A  
 preliminary comparison with the above model to RF model  $z_i$  estimates at SGP was very poor, as the radiosondes (from all  
 three methods) invariably pick up the nocturnal LLJ at SGP as the height of the boundary layer. Although the height of the  
 nocturnal boundary layer height could be debatable at SGP, the premise of this paper is to show the effectiveness of the RF  
 470 model in tracking and detecting the boundary layer height and the input boundary layer height provided to the model. Further  
 research needs to be conducted on providing widely acceptable nocturnal boundary layer height at SGP, and a trained RF  
 model can provide continuous boundary layer height estimates even in nocturnal conditions with acceptable levels of accuracy.

**Table 5: Key parameter/feature unbiased importance estimates during nighttime conditions**

Parameters/Features	% Importance
Monin-Obukhov Length	19.12%
Tucker Method $z_i$	11.49%
Soil Temperature	7.81%
Surface Air Temperature	7.56%
Dew Point Temperature	6.31%
Longwave Radiation	6.24%
Turbulence Kinetic Energy	5.21%
Net radiation	4.72%
Surface wind speed	4.28%
Surface wind direction	3.76%
Lidar Dissipation rate variance	3.54%
Surface friction velocity	3.45%
Cloud base height	3.40%
Shortwave radiation	3.26%

Others	< 10%
--------	-------

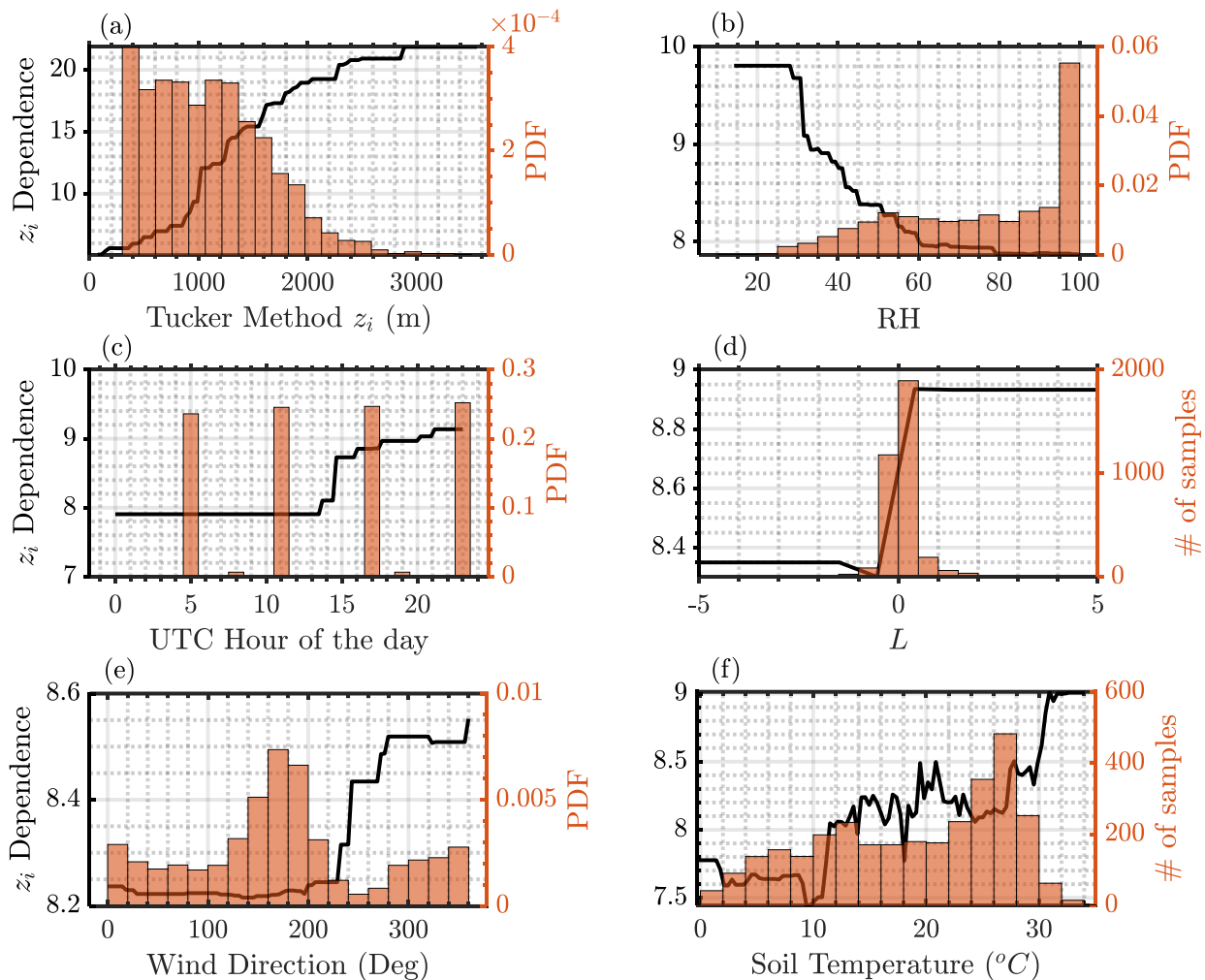
475

The partial dependence of key features on  $z_i$  during all conditions is shown in Figure 9. Partial dependence estimates show the marginal effect of features on the predicted outcome of an ML model. Therefore, a higher partial dependence estimate corresponds to higher sensitivity to the predicted outcome, in our case the boundary layer height and vice versa. From Figure 9, we see that RF model  $z_i$  is sensitive to warmer soil temperatures, lower relative humidity conditions, daytime hours, higher  $z_i$  from Tucker method, northerly wind directions, and stable atmospheric conditions. Most of these conditions would mimic dry convective conditions, with increased turbulence activity within the boundary layer. Monin-Obukhov length is observed to effectively categorize the training data into stable and unstable atmospheric conditions, with high partial dependence estimates during stable boundary layer conditions. Similar relationships can be derived for other parameters. It is important to note that the parameters shown to be important with respect to the RF model are features that successfully aid in the RF bagging process. Santenello et al., 2007 and Tang et al., 2018 showed parameters such as soil moisture and evaporative flux to be key variables in warm seasons, in a 2-parameteric regression framework, to affect boundary layer properties. Within the RF model, although those parameters are deemed important, soil temperature, lidar backscatter, and relative humidity were shown to have a higher impact on boundary layer height at each site.

In this research, the input features into the RF model are standard atmospheric parameters (such as wind speed, temperature etc.). An alternate approach to this effort would be to provide several non-dimensional inputs (such as Bulk Richardson number, Froud Number, etc) as inputs because they capture multiple dimensions of the data with a single variable (Vassallo et al., 2020). Because non-dimensional scaling is a common approach in atmospheric fluid dynamics to detect patterns in the data, a similar approach would provide the RF model with various relations and be helpful in classifying the data better. But further research needs to be conducted in defining the key nondimensional parameters that affect  $z_i$  and is a part of future work.

495





500 **Figure 9: RF partial dependence during all conditions from a) Tucker method  $z_i$ , b) relative humidity c) hour of the day, d) Monin-Obukhov Length, e) surface wind direction, and f) soil temperature to boundary layer height at the central facility. High dependence shows more sensitivity of the RF model to the bin of feature values.**

## 5 Normalized vertical velocity variance profiles

505 Within a convective boundary layer, vertical velocity variance profiles are often scaled by the convective velocity scale ( $w^*$ ), which is a function of  $z_i$  (Lenschow et al., 1980) for analysis. Therefore, any error in  $z_i$  estimates can result in altering the vertical velocity variance profiles. Herein, we attempt to estimate the effect of  $z_i$  on normalized vertical velocity variance profiles and convective velocity estimates, often used to compare results in boundary-layer studies and in the functional relationships used in atmospheric models. The convective velocity scale is given as

$$w^* = \left[ \frac{gz_i \overline{w'\theta'}}{\theta} \right]^{1/3} \quad (5)$$

510

where,  $g$  is the gravitational constant,  $\theta$  is potential temperature, and  $\overline{w'\theta'}$  is heat flux. The heat flux is obtained from the surface Eddy Covariance system at SGP C1 (Cook 2016) and potential temperature is measured at 4-m. An uncertainty in  $z_i$  will cause a non-linear effect in the convective velocity scale estimates. Assuming the uncertainty in  $z_i$  can be given as  $z_i'$ , and the mean is given as  $\bar{z}_i$ . The error caused in the convective velocity scale due to uncertainty in  $z_i$  can be formulated as shown below:

515

$$w^* = \left[ \frac{g(\bar{z}_i + z_i') \overline{w'\theta'}}{\theta} \right]^{1/3} \quad (6)$$

This can also be written as

$$520 \quad w^* = \left[ \frac{g\bar{z}_i \overline{w'\theta'}}{\theta} \right]^{1/3} \left( 1 + \frac{z_i'}{\bar{z}_i} \right)^{1/3} \quad (7)$$

Therefore, the convective velocity scale error due to uncertainty in  $z_i$  can be estimated using the term  $(1 + x)^{1/3}$ , where  $x = \frac{z_i'}{\bar{z}_i}$ . Based on observations at SGP C1,  $z_i$  from Tucker method is observed to be negatively biased to radiosonde estimates. The ratio,  $\left(\frac{z_i'}{\bar{z}_i}\right)$ , is calculated using the median error between Tucker method and RF model  $z_i$  by the median  $z_i$  using the RF model.

525

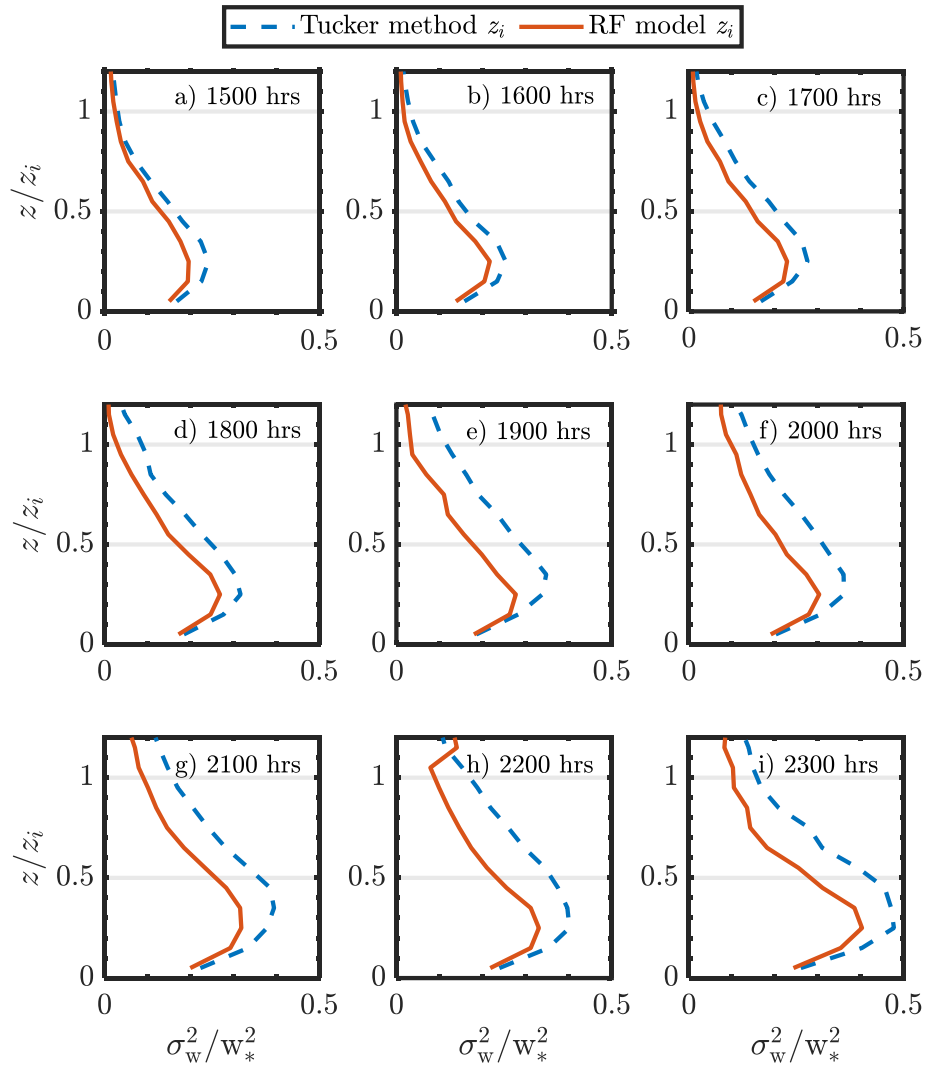
The ratio is calculated to be approximately -0.28 for data from 2016 to 2019. This would result in an uncertainty of approximately 10% in the convective velocity estimates when Tucker method  $z_i$  values are used in the calculations. Although this is an average, during certain conditions (e.g., during transition time periods) the effect of poor characterization of  $z_i$  can be even larger. Figure 10 shows average vertical velocity variance profiles during convective time periods at SGP from 2015 to 2019 using  $z_i$  estimates from Tucker method and RF model. Higher  $z_i$  values result in lower scaled vertical velocity variance estimates. Differences in variance profiles are observed to be smaller during daytime transition (1500 hours UTC or 0900 hours local time), as the Tucker method generally provides reliable  $z_i$  estimates. While during peak convective conditions (2000 hours UTC) and evening transition (2300 hours UTC), as observed earlier, the Tucker method  $z_i$  estimates tend to diverge from radiosonde  $z_i$  depending on the scenario and are negatively biased. Overall, the error introduced in the scaled vertical velocity variance profiles due to Tucker method  $z_i$  are above 15%.

530

535

As per definition, the turbulence at the top of the boundary layer is expected to be near zero, **except during cloudy conditions**. As shown in Figure 10, during morning transition periods, when the lidar does measure above the boundary layer, the scaled vertical velocity variance profiles do converge to zero. **In contrast**, during peak convective conditions the scaled profiles do not converge to zero and are observed to have an offset of generally around 0.1 at  $z_i$  (also observed in Lareau et al.,

2018). This could be due to higher uncertainty in lidar vertical velocity variance estimates near  $z_i$ , ineffective filtering of the  
 540 lidar false alarm rates (Bouquet et al., 2016), uncertainty in surface in situ measurements, and the possibility of residual  
 turbulence above the boundary layer during downdrafts/updrafts.



545 **Figure 10: Average normalized vertical velocity variance profiles during convection periods [1500 UTC to 2300 UTC (a-i)] at SGP from 2015 to 2019 versus non-dimensional height using Tucker method and RF model estimated  $z_i$ . Appropriate  $z_i$  (RF model or Tucker method) was used in both X and Y axis scaling.**

## 6 Case Study: Preliminary Model Comparisons

We expect the RF model  $z_i$  outputs to be developed into a VAP that will be easily accessible and can be used by  
550 researchers across the community. Therefore, the motivation for this case study is to provide a preliminary comparison  
between model estimated  $z_i$  and the RF model  $z_i$ . These types of comparisons will help understand the impact of boundary-  
layer properties on model physics and guide further in improving parameterizations used to represent boundary-layer  
turbulence.

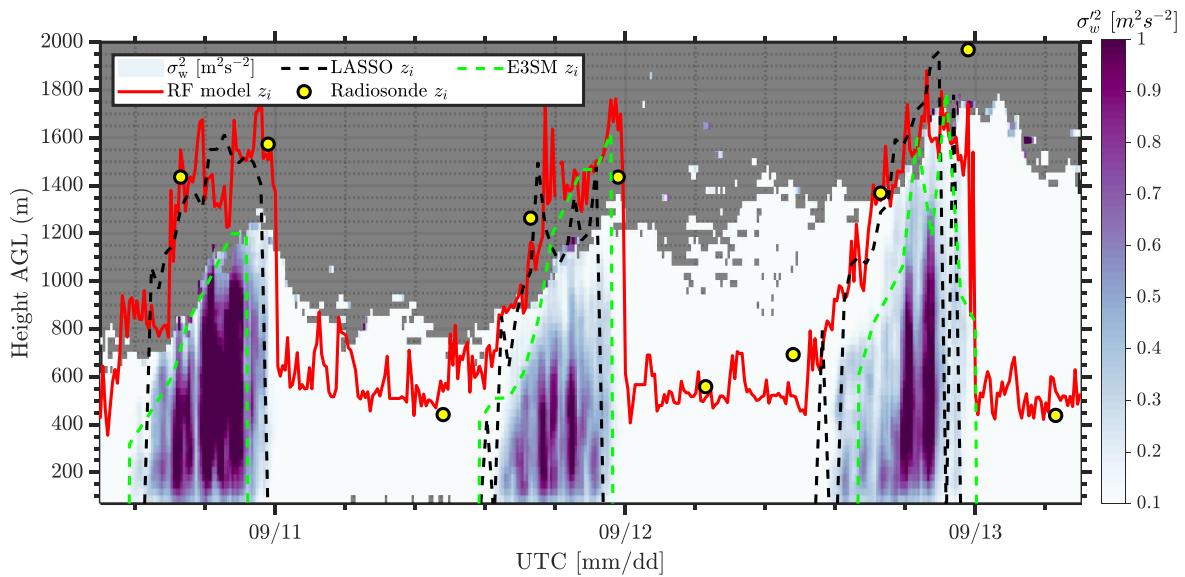
The surface and sub-surface layer measurements are key for understanding land-atmosphere interactions. Land-  
555 atmosphere interactions drive Earth's surface water and energy budgets. They can alter clouds and precipitation around a  
region, affect the growth of the planetary boundary layer height, and influence the persistence of extremes such as droughts.  
In view to better understand land-atmosphere interactions, a field campaign, Holistic Interactions of Shallow Clouds, Aerosols  
and Land Ecosystems (HI-SCALE), was conducted at the SGP site in Oklahoma (Fast et al., 2019). The field campaign was  
conducted from April to September of 2016, with two four-week intensive observational periods in May and September.  
560 Simulations were conducted on select clear sky days during the HI-SCALE field campaign. Two simulations using different  
modelling systems were performed: Energy Exascale Earth System Model (E3SM; Golaz et al., 2019) Atmosphere Model  
version 1 (EAMv1; Rasch et al. 2019), and a LES model. The Weather Research Forecasting (Skamarock et al. 2008) LES is  
set up in the same way as that used in operational LASSO (Gustafson et al., 2017, 2020). The Weather Research Forecasting  
model version used is v3.7. The model horizontal domain is square, doubly periodic, and 25.6 km wide with a 100-m horizontal  
565 grid spacing. The model top is set at 14.8 km above the surface. There are 226 vertical levels with a vertical grid spacing of  
~30 m in the lowest 5 km. The model is run for 15 hours for each case day starting at 6 AM. The Rapid Radiation Transfer  
Model for Global Climate Models parameterization is used for shortwave and longwave radiation (Clough et al. 2005; Iacono  
et al. 2008; Mlawer et al. 1997). The Thompson parameterization is used for microphysics (Thompson et al. 2004; 2008). The  
Deardorff 1.5-order turbulent kinetic energy approach is used for subgrid-scale parameterization (Deardorff 1980). The model  
570 is initialized with ARM sounding from the SGP site (ARM user facility, 2001). The surface sensible and latent heat fluxes are  
horizontally uniform and prescribed from the ARM constrained variational analysis data product (ARM user facility, 2004).  
The large-scale forcing is also taken from the ARM variational analysis data product. Due to high computational expense, the  
LES model was run for three days while EAMv1 model was run for the entire duration of the HISCALE campaign. The  
EAMv1 model is run in the standard coarse-resolution configuration with ~ 1-degree horizontal grid spacing and 72 vertical  
575 levels and a physics timestep of 30 minutes and a cloud and turbulence timestep of 5 minutes. In these models,  $z_i$  was estimated  
using resolved vertical velocity variance estimates from the LES or the parameterized vertical velocity estimate from the Cloud  
Layers Unified by Binormals (CLUBB) boundary-layer parameterization applied in E3SM (Golaz et al., 2002; Larson and  
Golaz, 2005; Bogenschutz et al., 2013; Larson, 2017), and like the Tucker method a low threshold was used to estimate the  
depth of the convective boundary layer. Estimates of boundary-layer height from E3SM and LASSO were not made during  
580 nocturnal conditions. The LASSO simulations extend only from approximately sunrise to sunset so nocturnal estimates of the

boundary-layer height are not possible. The E3SM simulations generally have too much nighttime turbulence, making estimates of the boundary-layer height unreliable at night.

Figure 11 shows Doppler lidar vertical velocity variance measurements for three days during the HI-SCALE campaign (September 10 – 12, 2016) and boundary layer height estimates from RF model, radiosondes, LASSO, and E3SM. 585 Because the RF model provides  $z_i$  estimates at a much finer temporal resolution than radiosondes, these estimates are ideal for comparing with models and assessing areas where model performance can be improved. Therefore, in this preliminary comparison, the primary motivation is to see if we can identify areas where the models diverge significantly by using near continuous accurate  $z_i$  values from the RF model. Due to computational expense, we could evaluate only three days of model results, but further research is needed in performing a thorough evaluation.

590 September 10<sup>th</sup> was relatively calm with northerly winds and no clouds were observed during daytime. September 11 and 12 had southerly winds and clear sky conditions during both daytime and nighttime. Daytime maximum surface air temperature is observed to increase progressively from September 10 to 12, and as mentioned earlier higher air temperature results in deeper planetary boundary layer due to increased convection (see Figure 11).

Overall, the LES model compares better to RF estimates, while EAMv1 is observed to underestimate  $z_i$ . Due to the 595 coarse resolution of EAMv1,  $\sim 100$  km,  $z_i$  estimates are averaged over a large domain and do not generally capture the fine scale variability. Although the LES model is observed to pick up morning transition, it diverges from observations during evening transitional periods and does not capture the decay of turbulence accurately. During peak convective conditions, when the vertical velocity variance is large, the LES is observed to correlate very well with the RF model and radiosonde  $z_i$ . Although EAMv1 is observed to mostly underestimate  $z_i$  compared to RF model estimates, occasionally the model captures the peak 600 convective trends. Like the LES model  $z_i$ , the EAMv1 also is not observed to capture evening decay of turbulence accurately but is observed to not track the early morning transition at SGP as well. Such systematic differences between the model and data are crucial for targeting future research directions. Further study is needed to evaluate the reasons why models tend to deviate during early morning and/or evening transition periods.



605

**Figure 11: Vertical velocity variance ( $\sigma_w^2$ ) estimates from Doppler lidar for three days [September 10, 11, and 12, 2016] with  $z_i$  estimates from a) RF model (red solid line), b) radiosondes (yellow circles), c) LASSO model (black dashed line), and d) E3SM model (green dashed line).**

## 610 6 Summary

This study used a range of near surface, sub-surface and Doppler lidar parameters to predict boundary layer heights at the ARM SGP site using an RF model. The RF model was trained using several years of data, and the model was validated with radiosonde estimates of boundary layer height. Because the Tucker method is observed to be low biased during peak convective periods due to low SNR of the Doppler lidars as the boundary layer deepens, the RF model corrects for the bias.

615 Seasonal and diurnal variations of  $z_i$  as observed from radiosondes correlate well with RF model  $z_i$ . During convective boundary layer conditions, the mean absolute error of boundary layer height estimated by the RF model is reduced by almost 50% compared to the Tucker method. Significant improvement was also observed during clear sky, and cloudy conditions. Nocturnal estimates from the RF model were not well correlated with radiosonde measurements, mostly due to near constant estimates of nocturnal boundary layer height at SGP (due to the presence of the LLJ). Moreover, valuable information on the

620 impact of surface parameters on nocturnal  $z_i$  estimates by the RF model provides avenues for further research in accurately estimating stable boundary layer heights at SGP. The key variables that have shown to have the largest impact on the RF model predictions are the initial guess of the boundary layer height from the Tucker method, hour of day, surface relative humidity, soil temperature, and attenuated backscatter (aerosol loading). During nocturnal conditions, several parameters, such as the Monin-Obukhov length, soil temperature, and surface air temperature influence the RF model estimates. These

625 parameters are aligned with theoretical parameterization schemes used to estimate boundary layer heights. The RF model used in this study explains around 82% of the variance in the data at SGP C1.

Uncertainty in convective boundary layer heights results in more than 10% difference in convective velocity scale estimates when the Tucker method is used. The uncertainty results in more than 15% error in scaled velocity variance estimates, which are commonly used in atmospheric models. Limited comparison between microscale model  $z_i$  estimates to  
630 RF model and radiosonde  $z_i$  values show increased correlation during heightened land-air interaction events. Large-eddy simulation estimates are observed to match the convective  $z_i$  variability as estimated by the RF model while the global model performance is variable. Neither models capture the evening transitional decay of turbulence accurately.

There are a number of ways to expand on the research presented here. Future work could focus on improved data imputation models to better handle missing data, a RF model  $z_i$  uncertainty framework using individual RF tree predictions,  
635 and finally a study of the effect of near-by wind farms and surface heterogeneity have on the boundary layer height.

## Appendix A

The range availability of the ARM SGP C1 Doppler lidars used in this study is provided below. Figure A1 shows the height range and data availability at SGP C1 for vertical stare scans and Figure A2 for processed VAD scans. The lidar range is consistent across multiple years of operation. The availability of data from the scanning Doppler lidars at SGP C1 is  
640 significantly reduced for altitudes greater 1 km (60% availability), which could limit its ability to reach the top of the boundary layer during all conditions.

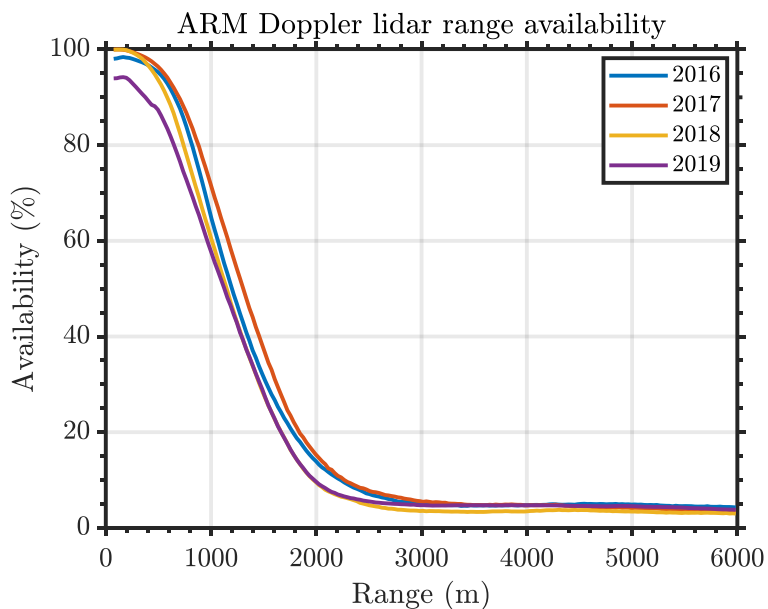
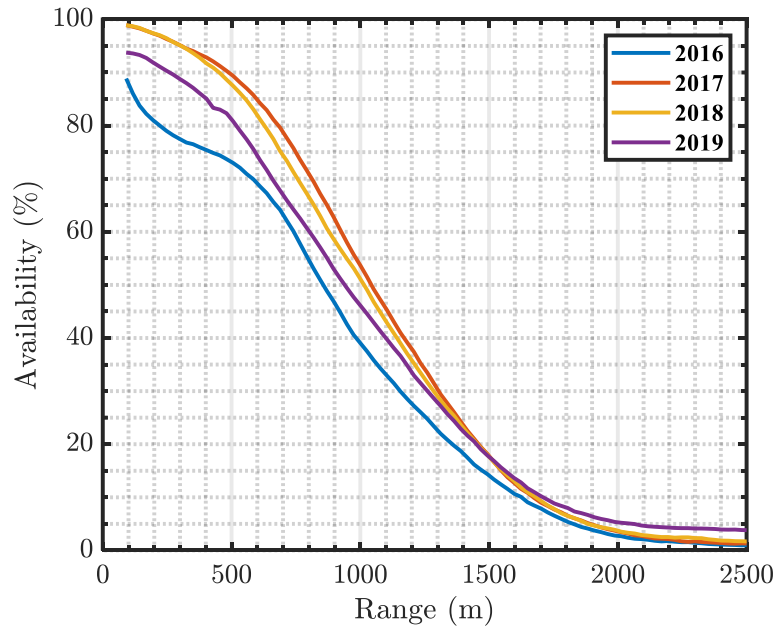


Figure A1: ARM SGP C1 Doppler lidar range availability versus range from vertical stares from 2016 to 2019 after SNR filtering (threshold of 1.008 dB).

645



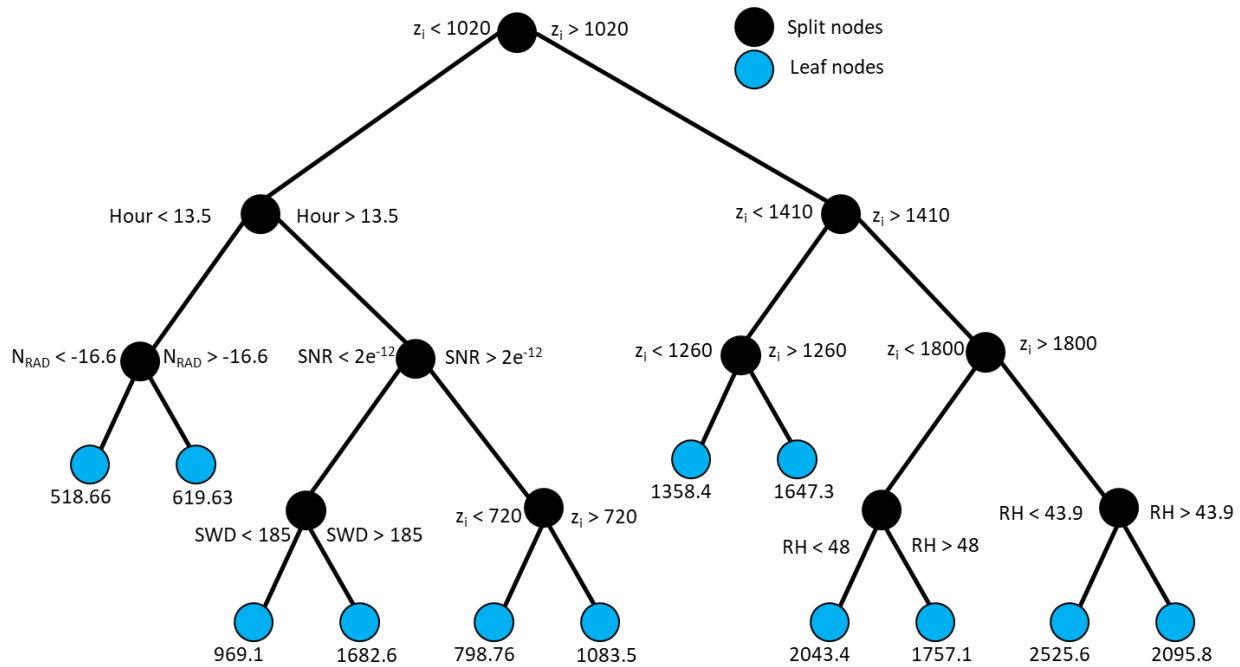


**Figure A2: ARM SGP C1 Doppler lidar wind speed profile range availability versus range using processed VAD scans from 2016 to 2019 after SNR filtering (threshold of 1.008 dB).**

650 **Appendix B**

The RF model develops several regression trees by regrouping the data based on several input features. Figure A1 below shows one of the trees developed by the model used in this article. The leaf nodes are the  $z_i$  estimates from radiosondes and the split nodes represent the surface and lidar data shown in Table 1. MATLAB built-in functions were used for the development of the RF model.

655



660 **Figure B1:** A sample regression tree developed by the RF model.  $Z_i$  is the Tucker method boundary layer height estimate, SNR is signal to noise ratio, NRAD is the normal radiation, RH is relative humidity, SWD is surface wind direction, Hour is hour of the day. The black circles represent the split nodes and the cyan circles represent the leaf nodes developed for this regression tree (aka boundary layer height estimates from radiosondes).

### Acknowledgements

665 The authors would like to acknowledge the support of Atmospheric Radiation Measurement (ARM) User Facility and the Atmospheric System Research (ASR) program for this research. The authors thank the ARM staff, instrument mentors for providing processed data, and guidance on the data archive. The authors also thank Dr. Duli Chand (PNNL), Dr. Joe Hardin (PNNL) and Dr. Christina Kumler (NOAA) for helpful discussions and comments on the manuscript. The Pacific Northwest National Laboratory is operated for the U.S. Department of Energy by Battelle under Contract DE-AC05-76RL01830.

### 670 Data Availability

All data used in this article are publicly available data on the ARM webpage. (<https://adc.arm.gov/discovery/#/>). Appropriate labels and manual citations for all the data used are provided in the manuscript.

### Author Contribution

675 RK and RN conceptualized the concept, RK, RN, and DDT were involved in the development of the algorithm, RK did the data processing and analysis of the RF algorithm, surface stations, lidar and radiosonde results, HX performed the large-eddy simulation runs, PM performed the E3SM runs, LB calculated the boundary layer height from model outputs, RK wrote the manuscript with contributions from all authors.

680 **Competing interests**

The authors declare no competing interests.

## References

- 685 Ackerman, T.P., Cress, T.S., Ferrell, W.R., Mather, J.H. and Turner, D.D., 2016. The programmatic maturation of the ARM Program. *Meteorological Monographs*, 57, pp.3-1.
- Arruda-Moreira, G., Guerrero-Rascado, J.L., Benavent Oltra, J.A., Ortiz-Amezcuca, P., Román, R., Bedoya-Velásquez, A.E., Bravo-Aranda, J.A., Olmo Reyes, F.J., Landulfo, E., and Alados Arboledas, L., 2019. Analyzing the turbulent planetary boundary layer by remote sensing systems: the Doppler wind lidar, aerosol elastic lidar and microwave radiometer. *Atmospheric measurement techniques*. 12(8), 4261–4276.
- 690 Atmospheric Radiation Measurement (ARM) User Facility. 2001. Updated hourly. Balloon-Borne Sounding System (SONDEWNP). Southern Great Plains (SGP) Central Facility, Lamont, OK (C1). Compiled by E. Keeler, M. Ritsche, R. Coulter, J. Kyrouac, and D. Holdridge. ARM Data Center. doi:10.5439/1021460.
- Atmospheric Radiation Measurement (ARM) User Facility. 2004. Constrained Variational Analysis (60VARANARUC). Southern Great Plains (SGP) Central Facility, Lamont, OK (C1). Compiled by C. Tao and S. Xie. ARM Data Center. doi:10.5439/1647300.
- 695 [Banakh, V. A., Smalikhov, I. N., and Falits, A. V. 2021. Estimation of the height of the turbulent mixing layer from data of Doppler lidar measurements using conical scanning by a probe beam. \*Atmospheric Measurement Techniques\*, 14\(2\), 1511-1524.](#)
- 700 Berg, L.K., Riihimaki, L.D., Qian, Y., Yan, H., and Huang, M. 2015. The low-level jet over the southern Great Plains determined from observations and reanalyses and its impact on moisture transport. *Journal of Climate*, 28(17), pp.6682-6706.
- Berg, L.K., Newsom, R.K. and Turner, D.D. 2017. Year-long vertical velocity statistics derived from Doppler lidar data for the continental convective boundary layer. *Journal of Applied Meteorology and Climatology*, 56(9), pp.2441-2454.
- Bianco, L., and Wilczak, J. M. 2002. Convective boundary layer depth: Improved measurement by Doppler radar wind profiler using fuzzy logic methods. *Journal of Atmospheric and Oceanic Technology*, 19(11), 1745-1758.
- 705 Bodini, N. and Optis, M. 2020. The importance of round-robin validation when assessing machine-learning-based vertical extrapolation of wind speeds. *Wind Energy Science*, 5(2), pp.489-501.
- Bonin, T. A., Carroll, B. J., Hardesty, R. M., Brewer, W. A., Hajny, K., Salmon, O. E., and Shepson, P. B. 2018. Doppler lidar observations of the mixing height in Indianapolis using an automated composite fuzzy logic approach. *Journal of Atmospheric and Oceanic Technology*, 35(3), 473-490.
- 710 [Boquet, M., Royer, P., Cariou, J. P., Machta, M., & Valla, M. \(2016\). Simulation of Doppler lidar measurement range and data availability. \*Journal of Atmospheric and Oceanic Technology\*, 33\(5\), 977-987.](#)
- Breiman, L. 2001. Random Forests. *Machine Learning*, 45 (1), pp. 5-32.
- Brooks, I.M. 2003. Finding boundary layer top: Application of a wavelet covariance transform to lidar backscatter profiles. *Journal of Atmospheric and Oceanic Technology*, 20(8), pp.1092-1105.
- 715 Brost, R.A. and Wyngaard, J.C. 1978. A model study of the stably stratified planetary boundary layer. *Journal of the Atmospheric Sciences*, 35(8), pp.1427-1440.
- Cadeddu, M.P., D.D. Turner, and J.C. Liljegren. 2009. A neural network for real-time retrievals of PWV and LWP from Arctic millimeter-wave ground-based observations. *IEEE Trans. Geosci. Remote Sens.*, 47, 1887-1900.
- 720 Campbell, J.R., D.L. Hlavka, E.J. Welton, C.J. Flynn, D.D. Turner, J.D. Spinhirne, V.S. Scott, and I.H. Hwang. 2002. Full-time, eye-safe cloud and aerosol lidar observations at Atmospheric Radiation Measurement program sites: Instruments and data processing. *J. Atmos. Oceanic Technol.*, 19, 431-442.
- Champagne, F.H., Friehe, C.A., LaRue, J.C., and Wynagaard, J.C., 1977. Flux measurements, flux estimation techniques, and fine-scale turbulence measurements in the unstable surface layer over land. *Journal of the atmospheric sciences*, 34(3), pp.515-530.
- 725

- Chen, Y., Zhang, S., Zhang, W., Peng, J. and Cai, Y. 2019. Multifactor spatio-temporal correlation model based on a combination of convolutional neural network and long short-term memory neural network for wind speed forecasting. *Energy Conversion and Management*, 185, pp.783-799.
- 730 Clough, SA, MW Shephard, E Mlawer, JS Delamere, M Iacono, K Cady-Pereira, S Boukabara, and PD Brown. 2005. Atmospheric radiative transfer modeling: A summary of the AER codes. *Journal of Quantative Spectroscopy and Radiative Transfer* 91: 233–244.
- Cohn, S.A. and Angevine, W.M. 2000. Boundary layer height and entrainment zone thickness measured by lidars and wind-profiling radars. *Journal of Applied Meteorology*, 39(8), pp.1233-1247.
- 735 Cook, D.R. 2018. Eddy correlation flux measurement system (ECOR) instrument handbook (No. DOE/SC-ARM-TR-052). DOE Office of Science Atmospheric Radiation Measurement (ARM) Program (United States).
- Cook, D.R. 2018. Soil Temperature and Moisture Profile (STAMP) System Instrument Handbook (No. DOE/SC-ARM-TR-186). DOE Office of Science Atmospheric Radiation Measurement (ARM) Program (United States).
- Cook, D.R., and Sullivan, R.C. 2019. Surface Energy Balance System (SEBS) Instrument Handbook (No. DOE/SC-ARM-TR-092). DOE Office of Science Atmospheric Radiation Measurement (ARM) Program (United States).
- 740 Dearnorff, JW. 1980. Stratocumulus-capped mixed layers derived from a 3-dimensional model. *Bound.-Layer Meteorology* 18: 495–527, doi:10.1007/Bf00119502.
- Emeis, S., Schäfer, K., and Münkel, C. 2008. Surface-based remote sensing of the mixing-layer height—a review. *Meteorologische Zeitschrift*, 17(5), pp.621-630.
- 745 Fast, J.D., Berg, L.K., Alexander, L., Bell, D., D’Ambro, E., Hubbe, J., Kuang, C., Liu, J., Long, C., Matthews, A., and Mei, F. 2019. Overview of the HI-SCALE field campaign: A new perspective on shallow convective clouds. *Bulletin of the American Meteorological Society*, 100(5), pp.821-840.
- Fernando, H.J.S. and Weil, J.C. 2010. Whither the stable boundary layer? A shift in the research agenda. *Bulletin of the American Meteorological Society*, 91(11), pp.1475-1484.
- 750 Gagne II, D.J., Haupt, S.E., Nychka, D.W., and Thompson, G. 2019. Interpretable deep learning for spatial analysis of severe hailstorms. *Monthly Weather Review*, 147(8), pp.2827-2845, <https://doi.org/10.1175/MWR-D-18-0316.1>
- Golaz, J.C., Larson, V.E., and Cotton, W.R., 2002. A PDF-based model for boundary layer clouds. Part I: Method and model description. *Journal of the atmospheric sciences*, 59(24), pp.3540-3551.
- 755 Grant, A.L.M. 1997. An observational study of the evening transition boundary-layer. *Quarterly Journal of the Royal Meteorological Society*, 123(539), pp.657-677.
- Gustafson, WI, AM Vogelmann, X Cheng, S Endo, B Krishna, Z Li, T Toto, and H Xiao. 2017. “Recommendations for Implementation of the LASSO Workflow.” Ed. by R. Stafford, DOE Atmospheric Radiation Measurement Climate Research Facility. DOE/SC-ARM-17-031, doi:10.2172/1406259.
- 760 Gustafson Jr, W.I., Vogelmann, A.M., Li, Z., Cheng, X., Dumas, K.K., Endo, S., Johnson, K.L., Krishna, B., Fairless, T., and Xiao, H. 2020. The Large-Eddy Simulation (LES) Atmospheric Radiation Measurement (ARM) Symbiotic Simulation and Observation (LASSO) Activity for Continental Shallow Convection. *Bulletin of the American Meteorological Society*, 101(4), pp. E462-E479.
- Han, C., Brdar, S., and Kollet, S. 2019. Response of Convective Boundary Layer and Shallow Cumulus to Soil Moisture Heterogeneity: A Large-Eddy Simulation Study. *Journal of advances in modeling earth systems*, 11(12), pp.4305-4322.
- 765 Hastie, T., Tibshirani, R., and Friedman, J., 2009. *The elements of statistical learning: data mining, inference, and prediction*. Springer Science & Business Media.
- Heffter, J.L. 1980, January. Transport layer depth calculations. In *Bulletin of the American Meteorological Society* (Vol. 61, No. 1, pp. 97-97). 45 BEACON ST, BOSTON, MA 02108-3693: AMER METEOROLOGICAL SOC.

- 770 Hennemuth, B. and Lammert, A., 2006. Determination of the atmospheric boundary layer height from radiosonde and lidar backscatter. *Boundary-Layer Meteorology*, 120(1), pp.181-200.
- Iacono, MJ, JS Delamere, EJ Mlawer, MW Shephard, SA Clough, and WD Collins. 2008. "Radiative forcing by long-lived greenhouse gases: Calculations with the AER radiative transfer models." *Journal of Geophysical Research* 113: D13103, doi:10.1029/2008jd009944.
- 775 Karlsson, J., Svensson, G., Cardoso, S., Teixeira, J., and Paradise, S. 2010. Subtropical cloud-regime transitions: Boundary layer depth and cloud-top height evolution in models and observations. *Journal of applied meteorology and climatology*, 49(9), pp.1845-1858.
- Knuteson, R. O., and coauthors. 2004. Atmospheric Emitted Radiance Interferometer. Part II: Instrument performance. *J. Atmos. Oceanic Technol.*, 21, 1777-1789
- 780 Krishnamurthy, R., Choukulkar, A., Calhoun, R., Fine, J., Oliver, A., & Barr, K. S. (2013). Coherent Doppler lidar for wind farm characterization. *Wind Energy*, 16(2), 189-206.
- Krishnamurthy, R., Newsom, R. K., Chand, D., and Shaw, W.J. (2020). Boundary Layer Climatology at ARM Southern Great Plains, PNNL-, Richland, WA: Pacific Northwest National Laboratory.
- Lareau, N.P., Zhang, Y., and Klein, S.A. 2018. Observed boundary layer controls on shallow cumulus at the ARM Southern Great Plains site. *Journal of the Atmospheric Sciences*, 75(7), pp.2235-2255.
- 785 Lareau, N.P. 2020. Subcloud and Cloud-Base Latent Heat Fluxes during Shallow Cumulus Convection. *Journal of the Atmospheric Sciences*, 77(3), 1081-1100.
- LeMone, M.A., Angevine, W.M., Bretherton, C.S., Chen, F., Dudhia, J., Fedorovich, E., Katsaros, K.B., Lenschow, D.H., Mahrt, L., Patton, E.G., and Sun, J. 2018. 100 years of progress in boundary layer meteorology. *Meteorological Monographs*, 59, pp.9-1.
- 790 Lenschow, D.H., Wyngaard, J.C., and Pennell, W.T. 1980. Mean-field and second-moment budgets in a baroclinic, convective boundary layer. *Journal of the Atmospheric Sciences*, 37(6), pp.1313-1326.
- Lenschow, D.H., Wulfmeyer, V., and Senff, C., 2000. Measuring second-through fourth-order moments in noisy data. *Journal of Atmospheric and Oceanic technology*, 17(10), pp.1330-1347.
- 795 Lenschow, D.H., Lothon, M., Mayor, S.D., Sullivan, P.P., and Canut, G., 2012. A comparison of higher-order vertical velocity moments in the convective boundary layer from lidar with in situ measurements and large-eddy simulation. *Boundary-layer meteorology*, 143(1), pp.107-123.
- Liu, S. and Liang, X.Z. 2010. Observed diurnal cycle climatology of planetary boundary layer height. *Journal of Climate*, 23(21), pp.5790-5809.
- 800 Markowski, P. and Richardson, Y. 2010. Organization of isolated convection. *Mesoscale meteorology in midlatitudes*, pp.201-244.
- Mather, J.H. and Voyles, J.W. 2013. The ARM Climate Research Facility: A review of structure and capabilities. *Bulletin of the American Meteorological Society*, 94(3), pp.377-392.
- Mather J, H Goss, and R Jundt. 2018. 2017 Annual Report. Ed. by Rolanda Jundt, ARM Climate Research Facility. DOE/SC-ARM-17-038.
- 805 McCord, R., and Voyles, J.W. 2016. The ARM data system and archive. *The Atmospheric Radiation Measurement Program: The First 20 Years*, Meteor. Monograph. Amer. Meteor. Soc. 57, 11.1-11.15.
- McGovern, A., Elmore, K.L., Gagne, D.J., Haupt, S.E., Karstens, C.D., Lagerquist, R., Smith, T., and Williams, J.K. 2017. Using artificial intelligence to improve real-time decision-making for high-impact weather. *Bulletin of the American Meteorological Society*, 98(10), pp.2073-2090.
- 810 McNicholas, C. and Turner, D.D. 2014. Characterizing the convective boundary layer turbulence with a High Spectral Resolution Lidar. *Journal of Geophysical Research: Atmospheres*, 119(22), pp.12-910.

- Mlawer, E.J., S.J. Taubman, P.D. Brown, M.J. Iacono, and S.A. Clough. 1997. "Radiative transfer for inhomogeneous atmospheres: RRTM, a validated correlated-k model for the longwave." *Journal of Geophysical Research* 102: 16663–16682, doi:10.1029/97jd00237.
- 815 Newsom, R.K., Turner, D.D., Mielke, B., Clayton, M., Ferrare, R., and Sivaraman, C. 2009. Simultaneous analog and photon counting detection for Raman lidar. *Applied optics*, 48(20), pp.3903-3914.
- Newsom, R.K., Sivaraman, C., Shippert, T.R., and Riihimaki, L.D. 2019a. Doppler Lidar WIND Value-Added Product (No. DOE/SC-ARM/TR-148). DOE Office of Science Atmospheric Radiation Measurement (ARM) Program (United States).
- 820 Newsom, R.K., Sivaraman, C., Shippert, T.R., and Riihimaki, L.D. 2019b. Doppler Lidar Vertical Velocity Statistics Value-Added Product (No. DOE/SC-ARM/TR-149). DOE Office of Science Atmospheric Radiation Measurement (ARM) Program (United States).
- Newsom, R.K. and Krishnamurthy, R. 2020. Doppler lidar (DL) handbook (No. DOE/SC-ARM/TR-101). DOE Office of Science Atmospheric Radiation Measurement (ARM) Program (United States).
- 825 Pearson, G., F. Davies, and C. Collier. 2009. An analysis of the performance of the UFAM pulsed Doppler lidar for observing the boundary layer. *J. Atmos. Oceanic Technol.*, 26, 240-250, doi:10.1175/2008JTECH1128.1
- Ramasamy, P., Chandell, S.S., and Yadav, A.K. 2015. Wind speed prediction in the mountainous region of India using an artificial neural network model. *Renewable Energy*, 80, pp.338-347.
- Rasch, P.J., Xie, S., Ma, P.L., Lin, W., Wang, H., Tang, Q., Burrows, S.M., Caldwell, P., Zhang, K., Easter, R.C., and Cameron-Smith, P. 2019. An overview of the atmospheric component of the Energy Exascale Earth System Model. *Journal of Advances in Modeling Earth Systems*, 11(8), pp.2377-2411.
- 830 Reif, D.W. and Bluestein, H.B. 2017. A 20-year climatology of nocturnal convection initiation over the central and southern Great Plains during the warm season. *Monthly Weather Review*, 145(5), pp.1615-1639.
- Ritsche, M. T., and Prell, J. 2011. ARM Surface Meteorology Systems (MET) Handbook, DOE/SC-ARM/TR-086. DOE Office of Science Atmospheric Radiation Measurement (ARM) Program (United States).
- 835 Santanello Jr, J.A., Friedl, M.A., and Kustas, W.P. 2005. An empirical investigation of convective planetary boundary layer evolution and its relationship with the land surface. *Journal of Applied Meteorology*, 44(6), pp.917-932.
- Santanello Jr, J.A., Friedl, M.A., and Ek, M.B. 2007. Convective planetary boundary layer interactions with the land surface at diurnal time scales: Diagnostics and feedbacks. *Journal of Hydrometeorology*, 8(5), pp.1082-1097.
- 840 Schween, J. H., Hirsikko, A., Löhnert, U., and Crewell, S. 2014. Mixing-layer height retrieval with ceilometer and Doppler lidar: from case studies to long-term assessment. *Atmospheric Measurement Techniques*, 7(11), 3685-3704.
- Seibert, P., Beyrich, F., Gryning, S.E., Joffre, S., Rasmussen, A., and Tercier, P. 2000. Review and intercomparison of operational methods for the determination of the mixing height. *Atmospheric environment*, 34(7), pp.1001-1027.
- 845 Sisterson, D.L, Peppler, R.A., Cress, T.S., Lamb, P.J., and Turner, D.D. 2016. The ARM Southern Great Plains (SGP) site. The Atmospheric Radiation Measurement Program: The First 20 Years, Meteor. Monograph. Amer. Meteor. Soc. 57, 6.1-6.14, DOI:10.1175/AMSMONOGRAPHS-D-16-0004.1
- Shukla, K. K., Phanikumar, D. V., Newsom, R. K., Kumar, K. N., Ratnam, M. V., Naja, M., and Singh, N. 2014. Estimation of the mixing layer height over a high altitude site in Central Himalayan region by using Doppler lidar. *Journal of Atmospheric and Solar-Terrestrial Physics*, 109, 48-53.
- 850 Sivaraman, C., McFarlane, S., Chapman, E., Jensen, M., Toto, T., Liu, S., and Fischer, M. 2013. Planetary Boundary Layer (PBL) Height Value Added Product (VAP): Radiosonde Retrievals. Department of Energy Office of Science Atmospheric Radiation Measurement (ARM) Program (United States).
- Solheim, F., Godwin, J.R., Westwater, E.R., Han, Y., Keihm, S.J., Marsh, K., and Ware, R. 1998. Radiometric profiling of temperature, water vapor, and cloud liquid water using various inversion methods. *Radio Sci.*, 33, 393-404



- 855 Sørensen, J.H., Rasmussen, A., Ellermann, T., and Lyck, E. 1998. Mesoscale influence on long-range transport—evidence from ETEX modelling and observations. *Atmospheric Environment*, 32(24), pp.4207-4217.
- Sawyer, V. and Li, Z. 2013. Detection, variations and intercomparison of the planetary boundary layer depth from radiosonde, lidar and infrared spectrometer. *Atmospheric Environment*, 79, pp.518-528.
- 860 Skamarock, WC, JB Klemp, J Dudhia, DO Gill, DM Barker, MG Duda, W Wang, and JG Powers. 2008. A description of the advanced research WRF version 3. NCAR Technical Note, NCAR/TN-475+STR, National Center for Atmospheric Research, 113 pp. doi:10.5065/D68S4MVH.
- Summa, D., Di Girolamo, P., Stelitano, D., and Cacciani, M., 2013. Characterization of the planetary boundary layer height and structure by Raman lidar: comparison of different approaches. *Atmospheric Measurement Techniques*, 6(12).
- 865 Sunny Lim, K.S., Riihimaki, L.D., Shi, Y., Flynn, D., Kleiss, J.M., Berg, L.K., Gustafson Jr, W.I., Zhang, Y., and Johnson, K.L. 2019. Long-term retrievals of cloud type and fair-weather shallow cumulus events at the ARM SGP site. *Journal of Atmospheric and Oceanic Technology*, 36(10), pp.2031-2043.
- Tang, Q., Xie, S., Zhang, Y., Phillips, T.J., Santanello, J.A., Cook, D.R., Riihimaki, L.D., and Gaustad, K.L. 2018. Heterogeneity in warm-season land-atmosphere coupling over the US Southern Great Plains. *Journal of Geophysical Research: Atmospheres*, 123(15), pp.7867-7882.
- 870 Tang, S., Xie, S., Zhang, Y., and Cook, D.R. 2019. The QCECOR Value-Added Product: Quality-Controlled Eddy Correlation Flux Measurements (No. DOE/SC-ARM-TR-223). DOE Office of Science Atmospheric Radiation Measurement (ARM) Program (United States).
- Teixeira, J. and Cheinet, S. 2004. A simple mixing length formulation for the eddy-diffusivity parameterization of dry convection. *Boundary-layer meteorology*, 110(3), pp.435-453.
- 875 Tibshirani, R. 1996. Regression shrinkage and selection via the lasso. *Journal of the Royal Statistical Society: Series B (Methodological)*, 58(1), pp.267-288.
- Thompson, G, RM Rasmussen, and K Manning, 2004. Explicit forecasts of winter precipitation using an improved bulk microphysics scheme. Part I: Description and sensitivity analysis. *Monthly Weather Review* 132: 519–542.
- Thompson, G, PR Field, RM Rasmussen, and WD Hall. 2008. Explicit forecasts of winter precipitation using an improved bulk microphysics scheme. Part II: Implementation of a new snow parameterization. *Monthly Weather Review* 136: 5095–5115.
- 880 [Träumner, K., Kottmeier, C., Corsmeier, U., and Wieser, A. 2011. Convective boundary-layer entrainment: Short review and progress using Doppler lidar. \*Boundary-layer meteorology\*, 141\(3\), 369-391.](#)
- 885 [Tucker, S.C., Senff, C.J., Weickmann, A.M., Brewer, W.A., Banta, R.M., Sandberg, S.P., Law, D.C., and Hardesty, R.M., 2009. Doppler lidar estimation of mixing height using turbulence, shear, and aerosol profiles. \*Journal of Atmospheric and Oceanic Technology\*, 26\(4\), pp.673-688.](#)
- Turner, D.D., Wulfmeyer, V., Berg, L.K., and Schween, J.H. 2014. Water vapor turbulence profiles in stationary continental convective mixed layers. *Journal of Geophysical Research: Atmospheres*, 119(19), pp.11-151.
- 890 Turner, D.D., Goldsmith, J.E.M., and Ferrare, R.A. 2016. Development and applications of the ARM Raman lidar. *The Atmospheric Radiation Measurement Program: The First 20 Years*, Meteor. Monograph, 57, Amer. Meteor. Soc., 18.1-18.15.
- Quan, J., Gao, Y., Zhang, Q., Tie, X., Cao, J., Han, S., Meng, J., Chen, P., and Zhao, D. 2013. Evolution of planetary boundary layer under different weather conditions, and its impact on aerosol concentrations. *Particuology*, 11(1), pp.34-40.
- 895 [Vakkari, V., O'Connor, E. J., Nisantzi, A., Mamouri, R. E., and Hadjimitsis, D. G. 2015. Low-level mixing height detection in coastal locations with a scanning Doppler lidar. \*Atmospheric Measurement Techniques\*, 8\(4\), 1875-1885.](#)
- Vassallo, D., Krishnamurthy, R., and Fernando, H.J. 2020. Decreasing wind speed extrapolation error via domain-specific feature extraction and selection. *Wind Energy Science*, 5(3), pp.959-975.

- Vassallo, D., Krishnamurthy, R., & Fernando, H. J. (2021). Utilizing physics-based input features within a machine learning model to predict wind speed forecasting error. *Wind Energy Science*, 6(1), 295-309.
- 900 von Engeln, A. and Teixeira, J. 2013. A planetary boundary layer height climatology derived from ECMWF reanalysis data. *Journal of Climate*, 26(17), pp.6575-6590.
- Weckworth, T.M., Spuler, S., and Turner, D.D. 2020. Micropulse Differential Absorption Lidar (MPD) Network Demonstration Field Campaign Report (No. DOE/SC-ARM-20-002). ARM Data Center, Oak Ridge National Laboratory (ORNL), Oak Ridge, TN (United States).
- 905 Wharton, S. and Lundquist, J.K. 2012. Assessing atmospheric stability and its impacts on rotor-disk wind characteristics at an onshore wind farm. *Wind Energy*, 15(4), 525-546.
- Wood, R. and Bretherton, C.S. 2004. Boundary layer depth, entrainment, and decoupling in the cloud-capped subtropical and tropical marine boundary layer. *Journal of climate*, 17(18), pp.3576-3588.
- Xie, SC, RT Cederwall, and MH Zhang. 2004. Developing long-term single-column model/cloud system-resolving model forcing data using numerical weather prediction products constrained by surface and top of the atmosphere observations. *Journal of Geophysical Research* 109: D01104.
- 910 [Yoo, W., Mayberry, R., Bae, S., Singh, K., He, Q. P., & Lillard Jr, J. W. \(2014\). A study of effects of multicollinearity in the multivariable analysis. \*International journal of applied science and technology\*, 4\(5\), 9.](#)
- Zhang, Y., Seidel, D.J., and Zhang, S. 2013. Trends in planetary boundary layer height over Europe. *Journal of climate*, 26(24), pp.10071-10076.
- 915 Zilitinkevich, S.S. 1972. On the determination of the height of the Ekman boundary layer. *Boundary-Layer Meteorology*, 3(2), pp.141-145.
- Zilitinkevich, S. and Baklanov, A. 2002. Calculation of the height of the stable boundary layer in practical applications. *Boundary-Layer Meteorology*, 105(3), pp.389-409.